Relating a Jet-Surface Interaction Experiment to a Commercial Supersonic Transport Aircraft Using Numerical Simulations

Vance F. Dippold, III[*] and David Friedlander[†]
NASA Glenn Research Center, Cleveland, Ohio, 44135

Reynolds-Averaged Navier-Stokes (RANS) simulations were performed for a commercial supersonic transport aircraft concept and experimental hardware models designed to represent the installed propulsion system of the conceptual aircraft in an upcoming test campaign. The purpose of the experiment is to determine the effects of jet-surface interactions from supersonic aircraft on airport community noise. RANS simulations of the commercial supersonic transport aircraft concept were performed to relate the representative experimental hardware to the actual aircraft. RANS screening simulations were performed on the proposed test hardware to verify that it would be free from potential rig noise and to predict the aerodynamic forces on the model hardware to assist with structural design. The simulations showed a large region of separated flow formed in a junction region of one of the experimental configurations. This was dissimilar with simulations of the aircraft and could invalidate the noise measurements. This configuration was modified and a subsequent RANS simulation showed that the size of the flow separation was greatly reduced. The aerodynamic forces found on the experimental models were found to be relatively small when compared to the expected loads from the model's own weight.

Nomenclature

C_D	=	Drag coefficient
C_L	=	Lift coefficient
D_{pr}	=	Diameter of primary stream nozzle
F_x, F_y, F_z	=	Forces in Cartesian directions
IDC	=	Inlet circumferential distortion
IDR	=	Inlet radial distortion
L/D	=	Ratio of lift to drag; C_L/C_D
M_∞	=	Freestream Mach number
NPR	=	Nozzle pressure ratio
NTR	=	Nozzle temperature ratio
p_0	=	Local total pressure
$p_{0,\infty}$	=	Freestream total pressure
$p_2/p_{0,\infty}$	=	Inlet total pressure recovery
p_∞	=	Freestream static pressure
S	=	Aircraft reference area
T_∞	=	Freestream static temperature
tke	=	Turbulent kinetic energy
u	=	Streamwise velocity
U_{jet}	=	Velocity of primary nozzle stream if ideally expanded
U_∞	=	Freestream velocity

[*] Aerospace Engineer, Inlets & Nozzles Branch, 21000 Brookpark Rd, and AIAA Senior Member
[†] Aerospace Engineer, Inlets & Nozzles Branch, 21000 Brookpark Rd, and AIAA Member

x, y, z	=	Cartesian coordinates
y^+	=	Non-dimensional wall distance
α	=	Aircraft angle of attack
Δn	=	Normal grid spacing along wall
ρ_∞	=	Freestream density

I. Introduction

NASA and industry partners desire to reintroduce commercial supersonic airliners to the air transportation system[1]. There are a number of technical challenges that must be overcome by future commercial supersonic airliners to make them viable solutions in society today. NASA is specifically concerned with the challenges of reducing sonic boom noise levels during supersonic cruise, maximizing range, and reducing airport community noise to acceptable levels[2]. Concepts for commercial supersonic transports, such as the aircraft developed by Lockheed Martin[3] pictured in Figure 1, place the engine nozzles in close proximity to wing and tail surfaces. However, the effects of noise shielding and noise radiation from these surfaces are not fully understood for installed propulsion systems. A series of acoustic tests are being conducted on the NASA Glenn Research Center's Nozzle Acoustic Test Rig (NATR) to address the challenge of reducing airport community noise[2], which is often dominated by jet noise. To best represent the conceptual aircraft in the acoustic tests, noise measurements will be taken of the jet in close proximity to representative aerodynamic surfaces, not simply of an isolated jet.

The purpose of the study discussed here was to use Reynolds-Averaged Navier Stokes (RANS) simulations to relate the nozzle flow of the conceptual commercial supersonic airliner (the LM1044-3) to the experimental jet-surface interaction model used on the NATR at take-off conditions. The RANS simulations of the NATR experimental configuration were also used to assure the flowfields in the experiment mimicked that of the full-scale aircraft and to compute the aerodynamic loads on the NATR model to be used for mechanical and structural design. Finally, the simulations of the LM1044-3 aircraft provided flow distortion patterns at the fan faces of the engines, allowing predictions of the inlet performance and fan noise in low-speed operation.

II. Geometries

A. LM1044-3 Concept Aircraft

The LM1044-3 concept aircraft, shown in Figure 2, is a supersonic passenger aircraft designed by Lockheed Martin under a NASA contract[3]. The LM1044-3 aircraft was designed to cruise at Mach 1.7. The aircraft consists of three engines mounted on pylons: two outboard engines, one under each wing, and a center engine, mounted on the upper surface of the aircraft. The center engine is rotated at a 2° angle of attack relative to the aircraft. Otherwise, each engine is internally identical. The inlet is an external-compression, axisymmetric spike inlet. It has a translating cowl that moves forward to open circumferential auxiliary doors for increased airflow at low speeds[3]. Each engine also has an inverted velocity profile (IVP), three-stream nozzle. RANS simulations of the isolated IVP nozzle were performed several years prior to the studies in this report; those simulations are discussed in detail in the Appendix. Moving outward from the IVP nozzle axis, the three streams include an inner stream, a primary stream, and a buffer stream. The primary stream is the largest stream and consists of mixed flow from the engine core stream and the secondary fan stream. The inner stream and buffer stream each consist of 50% of the flow from a tertiary fan stream. While the inner and primary streams span the entire circumference of the nozzle, the buffer stream spans only ground-side half of the nozzle circumference. The internal flowpaths of the IVP nozzle are proprietary, therefore the nozzle internals will be obscured in all figures. Like the inlet, the three stream nozzles also have a geometry that is varied throughout the flight envelope. For the inlets and nozzles, only the take-off configuration was used for the simulations in this study. Lastly, the inlets and nozzles were simplified for this study: no internal support geometry (e.g., struts) was modeled.

B. Jet-Surface Interaction Experiment Configurations

Initially, two jet-surface interaction configurations were explored for the NATR experiment – an outboard engine configuration and a center engine configuration – to represent the engine configurations on the LM1044-3 aircraft. The two NATR jet-surface interaction models are pictured in Figure 3 and Figure 4. Based on the diameter of the primary nozzle, the scale of the experimental hardware is about 1:8.2. Both configurations utilize the same nozzle, nacelle, and simplified NATR upstream rig hardware geometries. The outboard engine configuration is meant to mimic the outboard engine of the LM1044-3 aircraft and its surrounding surfaces, including the inboard surface, outboard engine pylon, and vertical tail. Likewise, the center engine is intended to mimic the center engine of the LM1044-3 aircraft and its surrounding surfaces, including the center pylon, inboard surfaces, outboard pylons, and vertical tails.

After the initial round of simulations, modifications were made to the center engine configuration to provide a third NATR jet-surface interaction configuration. The vertical tails were removed and the inboard surfaces were shortened in such a way that the leading edges were moved downstream approximately 28 inches, about 53% of the original chord length; the outboard pylons remained the same. The reasons for the modifications to the center engine configuration will be further discussed in Section V.

III. Numerical Modeling

A. FUN3D Flow Solver

FUN3D[4], a production flow and design code developed at the NASA Langley Research Center, was chosen as the flow solver for the simulations due to its ability to handle complex geometries modeled by unstructured grids. FUN3D is a node-based, finite volume Navier-Stokes solver and can solve both compressible and incompressible flow problems. All simulations used Menter's Shear Stress Transport (SST) turbulence model[5]. Also, each simulation used the Roe flux-difference splitting scheme[6] with the Van Leer flux-vector splitting scheme[7] for the left hand side. Most simulations used local time stepping, however, a time-accurate simulation was also performed for the NATR center engine configuration.

B. Flow Conditions

The simulations of the LM1044-3 aircraft and the NATR models used flow conditions appropriate for take-off.

1. LM1044-3 Flow Conditions

The simulations of the LM1044-3 aircraft at take-off required boundary conditions to be set for the freestream flow, the inlets, and the three-stream nozzles. The freestream flow was set to Mach 0.3 with a static pressure of 14.3 psi and a static temperature of 530° R. A massflow boundary condition was applied for the outflow of each the inlet, which was specified as 860 lbm/s. The flow conditions applied to the nozzles were similar to set-point '3350' used by Bridges[2]. The actual nozzle pressure ratios (NPRs) and nozzle temperature ratios (NTRs) are specified in Table 1. The ideally-expanded jet velocity (U_{jet}) of the primary stream, based on NPR=2.00, was 1469 ft/s.

Table 1: Nozzle flow conditions for LM1044-3 and NATR simulations.

Nozzle Stream	NPR	NTR
Inner	1.780	1.245
Primary	2.00	1.887
Buffer	1.780	1.245

During the wind tunnel testing reported by Morgenstern, et al[3], a model of the LM1044-2 aircraft (a design iteration prior to the LM1044-3) was tested at angles of attack from -6° to +15°, however the exact range of angles of attack during climb was not specified. It was assumed that the large angles of attack – near 15° – were intended for rotation during take-off. Therefore, angles of attack of 6° and 9° were assumed to be reasonable angles of attack for climb. Simulations of the LM1044-3 aircraft were performed at 0°, 6°, and 9° angles of attack in order to assess the impact of the aircraft's flight angle on flow separation and inlet performance.

2. Nozzle Acoustic Test Rig Model Flow Conditions

The NATR is significant because it can simulate forward flight up to Mach 0.35 using a 53 inch diameter freejet that exhausts just upstream of the nozzle rig[2]. To mimic the Mach 0.3 freestream flow of the LM1044-3 simulations, the NATR freejet was specified with a jet Mach number of 0.3 using a nozzle pressure ratio of 1.064. The freejet nozzle temperature ratio was specified as 1.018, for a jet static temperature of 530° R. Since the NATR models used a scale nozzle of the LM1044-3 three-stream IVP nozzle, the nozzle inflow conditions used the same conditions specified in Table 1. The farfield ambient conditions were treated as quiescent ambient conditions, with a Mach number of 0.01, a static pressure of 14.3 psi, and a static temperature of 530° R.

C. Grids

Unstructured grids were generated for the LM1044-3 aircraft and the NATR models for RANS simulations. The complexity of each geometry meant that unstructured grid techniques were best suited to successfully generate grids.

1. LM1044-3 Aircraft

An unstructured grid for the LM1044-3 aircraft was generated using Pointwise[8]. The grid took advantage of symmetry to reduce computational costs and consisted of only half of the LM1044-3 aircraft. However, all results are reported for the full aircraft. Viscous wall spacing – or the height of the first grid cell off of viscous surfaces – was set to 0.0001 inches, for a nominal y^+ value less than one. This helped ensure that the boundary layer would be sufficiently resolved. The grid farfield was located approximately 10 vehicle lengths away from the LM1044-3 aircraft in all directions (the LM1044-3 aircraft was approximately 2900 inches long). The grid consisted of 27.9 million nodes; it is pictured in Figure 5. To assess grid convergence of the RANS simulations, a second grid of the LM1044-3 was generated with the height of the first cell off of viscous surfaces increased to 0.0002 inches. All other aspects of the grid remained constant. The coarsened grid was composed of 27.2 million nodes.

The first LM1044-3 aircraft grid was not intentionally clustered in the jet plumes. This lead to unphysical-looking jet plumes, as will be further discussed in Section IV. Within Pointwise, zonal interface surfaces were placed along the expected shear layers of the nozzle in order to cluster grid points into these regions so that the shear layers would be sufficiently resolved. (Pointwise combines all zones into one large zone when exporting grids for FUN3D, so these zonal interfaces would likely not be actual zonal interfaces during the simulation.) The interface for the nozzle jet plumes extended from the lip of the nozzle's primary stream to about 12.5 nozzle diameters downstream. Grid spacing normal to the zonal interfaces was set to 0.001 inches. The grid of the LM1044-3 aircraft with refined jet plumes, pictured in Figure 6, consisted of 39.3 million nodes.

2. NATR Center Engine

The unstructured grid of the NATR center engine configuration was generated using Pointwise. This grid consisted of the full geometry – no symmetry conditions were used, even though the geometry was symmetric. Viscous wall spacing was set to 0.0002 inches along applicable walls, for a nominal value of y^+ between one and two. Similar to the plume refinement region added to the LM1044-3 jet plumes, zonal interfaces were added to the expected shear layers of the freejet and nozzle. The interface for the freejet extended from the freejet lip to a little over four freejet diameters downstream. The interface for the nozzle extended from the lip of the nozzle's primary stream to about 12.5 nozzle diameters downstream. Grid spacing normal to the zonal interfaces was set to 0.001 inches. The NATR center engine grid consisted of 51.1 million nodes; it is pictured in Figure 7.

Upon completing a RANS simulation of the original NATR center engine configuration, the configuration was redesigned. (The geometry was discussed in Section II; the reason for the modifications will be discussed in Section V.) A new unstructured grid was generated for the redesigned NATR center engine configuration in a procedure similar to how the original NATR center engine grid was generated. The grid for the redesigned NATR center engine configuration consisted of 27.7 million nodes. The significant reduction in grid nodes – nearly 46% – was the result of the removal of the vertical tails and shortened inboard surface. With less surface area, fewer near-surface grid nodes were required.

4

Furthermore, the surface mesh was found to be overly fine on non-critical surfaces (i.e., upstream rig support, freejet, etc.); the new grid reduced the number of points along (and near) these surfaces. The grid is pictured in Figure 8.

3. NATR Outboard Engine

Using the geometries discussed Section II, an unstructured grid was constructed for the NATR outboard engine configuration using a combination of Pointwise and AFLR3[9-11]. AFLR3 is a research code developed at Mississippi State University that uses the Advancing-Front/Local-Reconstruction method for generating unstructured tetrahedral volume grids. For the NATR outboard engine configuration, Pointwise was used to generate the surface mesh; AFLR3 was used to generate the volume mesh. The grid for the NATR outboard engine was one of the first grids generated for this study, and AFLR3 was used to generate the volume grid because early attempts to generate a volume grid within Pointwise were unsuccessful. Once volume grids were successfully generated using Pointwise, the decision was made to use Pointwise for the remaining grids as Pointwise offered greater control of volume grid generation. The initial viscous spacing parameter within AFLR3 was set to 0.0001 inches. The resulting NATR outboard engine configuration grid had a total of 18.9 million nodes and is shown in Figure 9. It should be noted that the grid for the NATR outboard engine had considerably fewer nodes than the NATR center engine due to the fact that the grid points were not concentrated in the jet plume region.

D. Simulation Convergence

All simulations were completed on the multi-node, multi-core NASA Advanced Supercomputing (NAS) Pleiades supercomputer[12]. Each simulation used between 100 and 300 processor cores (depending upon the grid size). The simulations were run as steady-state, with a global CFL number. For nearly all cases, the CFL number was increased from a value of 0.5 at start-up to a final CFL number of 5.0 or 10.0. The NATR center engine simulation showed signs of unsteady behaviors – the surface forces fluctuated and would not monotonically converge. Therefore, the NATR center engine model simulations were run time-accurate, with a constant time step. The time-accurate NATR model simulations used a time step of 1×10^{-5} seconds. FUN3D uses a dual time-stepping method. These time accurate simulations used five sub-iterations per time step with a CFL number of 5.0.

As the simulations were performed, convergence was monitored in multiple ways. The residuals of the RANS and turbulence model equations were monitored. For converged solutions, the residuals had to decrease by several orders of magnitude. Second, the surface forces were monitored. When the surface forces did not change significantly over hundreds to thousands of iterations, it was a sign that the solution was converged. Lastly, the solution flowfield was monitored. Once the flowfield showed no significant change and looked physical, the solution was deemed converged.

IV. Results of the LM1044-3 Aircraft Simulations

This section discusses RANS simulations performed of the LM1044-3 aircraft at take-off conditions. These simulations provided reference points that simulations of the jet-surface interaction experiment hardware, which were designed to mimic the LM1044-3 aircraft, could be related to.

A. Grid Convergence Study

A grid convergence study was conducted using two grids of the LM1044-3 aircraft that differed only in the prescribed initial grid cell height along viscous surfaces. The first grid used an initial viscous spacing of 0.0001 inches; the second, coarsened, grid used an initial viscous spacing of 0.0002 inches. The lift and drag coefficients were computed according to Equations 1 and 2:

$$C_L = \frac{-F_x \times \sin \alpha + F_z \times \cos \alpha}{\frac{1}{2} \times \rho_\infty \times (U_\infty)^2 \times S} \qquad \text{Eq. 1}$$

$$C_D = \frac{F_x \times \cos \alpha + F_z \times \sin \alpha}{\frac{1}{2} \times \rho_\infty \times (U_\infty)^2 \times S} \qquad \text{Eq. 2}$$

The total body forces on the airframe surfaces (i.e., not including the engine nacelles, inlets, or nozzles) are represented by F_x and F_z in the respective *x*- and *z*-directions, according to the axis in Figure 2.

The aircraft's angle of attack, α, was 0° for these initial simulations. The freestream density and velocity, represented by ρ_∞ and U_∞, were 2.2642×10^{-3} slug/ft^3 and 338.52 ft/s, respectively. The wing reference area, S, was 3600 ft^2, as specified by Morgenstern, et al[3]. The lift and drag coefficients for the regular and coarsened grids are shown in Table 2. The ratio of lift-to-drag is also shown. There was less than a 0.2% difference in drag and only a 1.5% difference in lift between the solutions on the two different grids. Furthermore, the flow solutions – in particular, pockets of separated flow near the engine nacelles, shown in Figure 10 – looked qualitatively similar. Therefore, it was concluded that the solution was nearly grid converged and that the grid with the initial viscous spacing of 0.0001 inches was adequate for further simulations.

Table 2: Lift and drag coefficients for regular and coarse grids of LM1044-3 aircraft. (Note that the engine nacelle surfaces, inlets, and nozzles were not included in the calculation.)

	Regular Grid (Δn=0.0001 in)	Coarsened Grid (Δn=0.0002 in)	Difference
C_L	0.0175	0.0172	1.51%
C_D	0.0060	0.0061	-0.18%
L/D	2.89	2.84	1.69%

B. LM1044-3

RANS simulations were performed of the LM1044-3 aircraft for a freestream Mach number of 0.3 and a 0° angle of attack. Figure 11 shows contours of the non-dimensionalized streamwise velocity, u/U_{jet}, along the vertical center plane through each engine (for $u/U_{jet} \geq 0.3$), in which U_{jet}=1469 ft/s. Additionally, iso-surfaces are plotted to indicate separated flow ($u<0$). Overall, the flow over the aircraft looks fairly clean, with only small regions of separated flow near the inlet auxiliary doors, along the engine pylon and aircraft body junctions, and on the nozzle plug. Of particular interest are the junctions between the engine nacelles, pylons, and wing and tail surfaces. As will be discussed in detail later, the junction region of the NATR center engine model was found to experience significant flow separation caused by the nacelle being much larger than the LM1044-3 engine nacelle. This can be seen by comparing the aircraft center engine nacelle in Figure 2 with that of the test hardware equivalent in Figure 4a. The simulation of the LM1044-3 shows that these junction regions are free of major flow separations.

The simulation of the LM1044-3 does show one weakness: the jet plumes decay extremely early when compared to RANS simulations of the isolated three-stream inverted velocity profile (IVP) nozzle discussed in the Appendix. The simulations of the isolated IVP nozzle, while they did not use the exact the same flow conditions as used for the simulations of the LM1044-3, are similar enough to show the approximate structure of the jet plume. Figure 12 shows that the jet potential core has ended before the jet plume travels the length of the plug. Furthermore, as shown in the plot of contours of turbulent kinetic energy in Figure 13, the simulation predicts virtually no turbulent kinetic energy in the jet plume. Since the successor of this study is focused on understanding the noise from a configuration similar to the LM1044-3, it is imperative that simulations of the LM1044-3 resolve the jet plume, including the velocity field and the turbulent kinetic energy field, which is directly related to jet noise.

C. LM1044-3 with Refined Plume Grid

A new grid was generated for the LM1044-3 with a region of refined grid in each jet plume and RANS simulations were performed using this refined plume grid. Figure 14 shows contours of streamwise velocity, u, along the vertical center plane through each engine (for $u/U_{jet} \geq 0.3$). Figure 15 and Figure 16 show contours of velocity and turbulent kinetic energy near the jet plumes, respectively. The refined plume grid does a much better job of resolving the jet plumes than the previous of grid. The center engine jet potential core extends downstream approximately 4.3 times the diameter of the primary stream nozzle, D_{pr}; the outboard engine jet potential core extends downstream about 3.9×D_{pr}. There seem to be no other changes in flow around the engine-pylon-wing junction. While the addition of grid points to the jet plume – especially the shear layer – greatly help to resolve and extend the jet plumes, Figure 17 shows that the jet

plumes do end just downstream of the end of the plume refined grid region. A truly grid-independent solution would likely require that the refined plume grid extend further downstream of each nozzle.

D. LM1044-3 at Angle of Attack

Simulations of the LM1044-3 aircraft model were also run for angles of attack of 6° and 9°, approximating the angle of attack that the aircraft would fly at during climb just after take-off. The primary goal was to observe if flow separation increased around the top-mounted center engine as the angle of attack increased. A secondary purpose was to use the results to assess the performance of the axisymmetric inlet. In Figure 18, regions of separated flow near the aft portion of the LM1044-3 aircraft are plotted and compared for each angle of attack: 0°, 6°, and 9°. The size and shape of the small regions of flow separation do not noticeably change as the angle of attack is increased from 0° to 9°. The simulated freestream flow around the NATR test model cannot be given an angle of attack. Therefore, this comparison performed for the LM1044-3 shows that the angle of attack at climb will not significantly affect flow separation around the engines, thus reinforcing the relevancy of the NATR model.

The performance of the LM1044-3 inlets was assessed as the aircraft angle of attack was increased. Inlet distortion and total pressure recovery were computed using 40 equal area-weighted probe points positioned just downstream of the diffuser. Contour plots of total pressure at the probe points are shown in Figure 19. Circumferential inlet distortion (IDC), radial inlet distortion (IDR), and face area averaged total pressure (p_2) were calculated according to the General Electric "Method D" Distortion Methodology found in Appendix II of Reference 13. The total pressure recovery ($p_2/p_{0,\infty}$) is the ratio of the face area average total pressure (p_2) to the freestream total pressure ($p_{0,\infty}$). The inlet distortions and total pressure recovery are listed for each inlet and each angle of attack in Table 3. The most significant change in inlet performance as angle is increased from 0° to 9° is observed for the outboard engine inlet IDC, which increases from 1.2% to 1.9%. For the outboard engine inlet, IDR remains constant as angle of attack increases of this range. For the center engine inlet, IDC and IDR remain nearly constant as angle of attack increases from 0° to 9°. The total pressure recovery ($p_2/p_{0,\infty}$) also changes very little as angle of attack is increased from 0° to 9°. At 0° angle of attack, the total pressure recovery of 99.2% to 99.3% shows good agreement with the total pressure recovery of 98.9% listed by Morgenstern, et al[3], helping to validate these RANS simulations.

Table 3: Performance of LM1044-3 inlet as angle of attack is increased for M_∞=0.3.

Angle of Attack (α)	0°	6°	9°
Center Engine			
Circumferential Inlet Distortion (IDC)	0.01184	0.01137	0.01101
Radial Inlet Distortion (IDR)	0.00376	0.00398	0.00410
Total Pressure Recovery ($p_2/p_{0,\infty}$)	0.99189	0.99111	0.99063
Outboard Engine			
Circumferential Inlet Distortion (IDC)	0.01216	0.01654	0.01915
Radial Inlet Distortion (IDR)	0.00610	0.00605	0.00612
Total Pressure Recovery ($p_2/p_{0,\infty}$)	0.99264	0.99239	0.99206

V. Results of the NATR Jet-Surface Interaction Model Simulations

This section discusses RANS simulations performed of the NATR jet-surface interaction experiment hardware. These simulations served as screening simulations of the experimental geometries before hardware was manufactured, to ensure that the experimental hardware was free of any potential sources of rig noise and to predict the loads on the aerodynamic surfaces for structural design. These simulations were also compared to the simulations performed for the LM1044-3 aircraft in order to show how the experimental configuration successfully mimicked the aircraft and how it differed.

A. NATR Center Engine

RANS simulations were performed of the NATR center engine configuration to determine the aerodynamic loads for the model's mechanical design and to screen the design for potential sources of rig noise. Figure 20a shows the convergence of the aerodynamic loads for the inboard surfaces for the NATR

center engine RANS simulation run in steady-state mode. (Refer to Figure 4a for geometry naming conventions.) The oscillations in the loads indicate that the simulation may be unsteady, rather than steady. Therefore, a time-accurate RANS simulation was run, using a global time step of 1×10^{-5} seconds. Figure 20b shows the convergence of the aerodynamic loads for the inboard surfaces of the NATR center engine configuration. The aerodynamics loads do develop a periodic behavior. Table 4 shows the average, maximum, and minimum aerodynamic loads for time-accurate simulation of the NATR center engine configuration. The ensemble-average aerodynamic loads from the steady-state (global CFL number) simulation are also shown in Table 4 for comparison. The time-accurate simulation to obtain the aerodynamic loads was the most thorough, but the additional simulation time doubled the computational cost. Because the forces were relatively small when compared to the expected weight of the test rig, it was determined that the ensemble-averaged loads from the steady-state simulation would be sufficient for future simulations.

Table 4: Aerodynamic loads for NATR center engine configuration.

Component	F_x [lb] Unsteady			F_x [lb] Steady	F_y [lb] Unsteady			F_y [lb] Steady	F_z [lb] Unsteady			F_z [lb] Steady
	Avg	Min	Max	Avg	Avg	Min	Max	Avg	Avg	Min	Max	Avg
Center Pylon	0.26	-0.28	0.78	0.48	-0.05	-0.13	0.01	-0.05	-2.04	-16.12	12.90	-2.63
Inboard Surfaces (pair)	2.09	-0.46	4.95	3.51	-0.21	-2.62	4.04	-0.19	-1.91	-43.57	43.43	-3.89
Nacelle	14.82	-1.65	23.09	12.61	0.46	-9.43	7.33	-0.51	24.23	11.11	40.84	25.10
Outboard Pylons (pair)	5.77	3.76	8.69	5.57	-0.72	-5.08	4.04	-0.02	6.13	-9.01	17.18	10.15
Tails (pair)	-0.90	-9.27	15.28	3.11	-1.63	-29.07	36.08	-0.58	-8.42	-73.76	91.33	10.27

A second purpose of the RANS simulation of the NATR center engine configuration was to screen the design for similitude with the LM1044-3 aircraft. Figure 21 and Figure 22 shows contour plots of streamwise velocity and turbulent kinetic energy along the vertical symmetry plan through the nozzle. As with the results of the LM1044-3 simulations, the streamwise velocity and turbulent kinetic energy are non-dimensionalized using the ideally-expanded jet velocity, U_{jet}=1469 ft/s. The jet plume along the center pylon appears to be well behaved and does not produce any undesirable turbulent kinetic energy. Figure 23 and Figure 24 show velocity contours and turbulent kinetic energy contours at a series of cross-planes along the NATR center engine configuration. In the plot of velocity contours (Figure 23), a region of separated flow develops on either side of the engine along the nacelle-pylon-inboard surface junction, from x=-25 inches to x=-15 inches. A pocket of turbulent kinetic energy develops in this region, too, indicating a potential source of rig noise not found in the actual aircraft being simulated. Figure 25 shows the region of separated flow in the NATR center engine configuration as an iso-surface of u<0, colored by turbulent kinetic energy contours.

The flow separation here is caused by the growing boundary layer in the corner between the NATR rig and the inboard surface that undergoes an unfavorable pressure gradient as the NATR rig transitions to the nozzle. Recalling Figure 11, the separated flow observed on the NATR center engine configuration was not observed on the LM1044-3. This is because the size of the NATR rig upstream of the nozzle is much larger than the LM1044-3 engine nacelle, when compared to the diameter of the nozzle's primary stream. The size of the NATR-scale nozzle was determined by the mass flow of the NATR, which is 30 lbm/s (combined flow). The nozzle primary stream diameter (D_{pr}) was used to scale the rest of the NATR center engine model, including the distance between the nozzle and center pylon. However, the diameter of the NATR rig upstream of the nozzle was fixed. Whereas the ratio of the outer diameter of the nacelle to the diameter of the primary stream nozzle is approximately 1.33:1 for the LM1044-3 aircraft, the ratio of the outer diameter of the jet rig to the diameter of the primary stream nozzle is approximately 2.53:1 for the NATR model. This results in the NATR jet rig being nearly $1.2\times D_{pr}$ larger than an ideally-scaled model. This is likely the largest difference between the NATR center engine configuration and the LM1044-3's center engine. There is a similar difference between the NATR outboard engine configuration and the LM1044-3's outboard engines.

B. Modified NATR Center Engine

The NATR center engine configuration was redesigned to reduce the region of separated flow at the nacelle-pylon-inboard surface junction. As shown in Figure 4b, the inboard surfaces were shortened by moving the leading edge downstream by approximately 28 inches, about 53% of the chord length. Additionally, the tail surfaces were removed from the configuration to simplify the model. Figure 26 and Figure 27 show contours of velocity and turbulent kinetic energy at a series of cross-planes along the NATR center engine configuration with shortened inboard surface. Compared to Figures 23 and 24, the region of separated flow is moved downstream (from -30 inches to -14 inches) and is reduced in size (from about 14 inches long to about 4 inches long); the peak turbulent kinetic energy from the flow separation has been reduced as well, from $tke/(U_{jet})^2$=0.0021 to $tke/(U_{jet})^2$=0.0008. Figure 28 shows iso-surfaces indicating the flow separation (u<0) on the redesigned NATR center engine model. Again, when compared to Figure 25, the region of separated flow is much smaller for the redesigned NATR center engine configuration. The ensemble-averaged aerodynamic loads for the redesigned configuration are listed in Table 5.

Table 5: Aerodynamic loads for modified NATR center engine configuration.

Component	F_x [lb]			F_y [lb]			F_z [lb]		
	Avg	Min	Max	Avg	Min	Max	Avg	Min	Max
Center Pylon	0.77	0.51	1.03	-0.05	-0.07	-0.03	-1.14	-2.99	1.03
Inboard Surfaces (pair)	3.39	0.63	6.32	-0.27	-0.82	0.60	8.93	-4.39	24.47
Nacelle	11.58	5.13	16.23	0.08	-1.44	1.64	2.72	-0.77	5.92
Outboard Pylons (pair)	7.06	5.39	8.49	-0.17	1.43	1.14	8.94	5.17	12.97

C. NATR Outboard Engine

A RANS simulation of the NATR outboard engine configuration was performed in a similar fashion as the NATR center engine configuration. The aerodynamic loads for the NATR outboard engine configuration were computed for the surfaces defined in Figure 3. Similar to the NATR center engine configuration, the total forces on the components did not completely converge, but varied as the simulation iterated. The forces were ensemble-averaged over the last 10,000 iterations of the simulation. The ensemble average, minimum, and maximum forces are listed in Table 6. From this data it can be seen that the loads are relatively small in magnitude, especially compared to the weight of the test rig, and therefore were not a concern to the experimentalist.

Table 6: Aerodynamic loads for the NATR outboard engine configuration.

Component	F_x [lb]			F_y [lb]			F_z [lb]		
	Avg	Min	Max	Avg	Min	Max	Avg	Min	Max
Vertical Tail	4.59	4.59	4.59	-1.01	-0.99	-1.02	2.25	2.23	2.26
Pylon	6.77	6.77	6.77	-2.02	-2.02	-2.03	2.40	2.39	2.40
Inboard Surface	6.98	6.98	6.98	4.94	4.93	4.95	-17.27	-17.24	-17.29
Nacelle	-0.41	-0.40	-0.41	1.86	1.86	1.87	-0.42	-0.42	-0.43

In addition to estimating the aerodynamic loads, the flow solution was interrogated to see if there were any potential sources of rig noise. The streamwise velocity and turbulent kinetic energy are plotted at a sequence of streamwise stations, as shown in Figure 29 and Figure 30. It can be seen from the streamwise plots, from x=-20 inches to x=25 inches, that there are no separation regions around the inboard surface junction with the rig support, nacelle, or pylon. For orientation, Figure 29 and Figure 30 show the inboard surface to the right of the pylon. Because there are no computed separation regions in the inboard surface junction areas, the levels of corresponding turbulent kinetic energy are relatively low, which predicts that the junction regions will not be a source of unrealistic noise for the NATR outboard engine test configuration.

VI. Conclusions

Reynolds-Averaged Navier-Stokes (RANS) simulations were performed at take-off flow conditions for the LM1044-3 commercial supersonic aircraft concept and hardware for a jet-surface interaction experiment designed to represent the propulsion and airframe integration of the LM1044-3

aircraft. The jet-surface interaction experiment was conducted in the Nozzle Acoustic Test Rig (NATR) at the NASA Glenn Research Center. The purposes of these RANS simulations were as follows:

- Relate the experimental hardware models to the LM1044-3 aircraft.
- Screen the experimental hardware for potential sources of rig noise.
- Estimate the aerodynamic loads on the experimental hardware for structural design.
- Provide estimates of the inlet flow distortions for inlet performance and fan noise analysis.

The RANS simulations of the LM1044-3 aircraft showed that the flow in the region of the center and outboard engine nacelles behaved well, with only a few small regions of flow separation on the inlet auxiliary doors, on the pylon near the inlet, and on the nozzle splitters and plug. The NATR models had a much larger "nacelle" (jet rig support) relative to the nozzle exit diameter than the LM1044-3 aircraft. The large adverse pressure gradient from the boattail of the oversized nacelle, coupled with the corner flow between the nacelle and the inboard surface, produced a large region of separated flow in the junction region of the original NATR center engine model. The modified NATR center engine model shortened the upstream length of the inboard surface and significantly reduced the size of the flow separation region. This was one significant difference found between the NATR center engine model and the LM1044-3 aircraft. The flow around the NATR outboard engine model was also free of flow separations, similar to the LM1044-3 outboard engine. The NATR has the ability to simulate forward flight around the jet rig, but is limited to an angle of attack of 0°. RANS simulations of the LM1044-3 at angles of attack of 0°, 6° and 9° showed no significant change in the flow around the engine nacelles, meaning that the NATR's angle of attack limitation would not significantly affect how well the NATR models should serve as a good representation of the LM1044-3 aircraft's installed propulsion system.

The RANS simulations of the NATR models showed that the NATR outboard engine model was free of phenomena that would generate noise that would not be found on the full-scale aircraft. The RANS simulations of the NATR center engine model found a large region of flow separation in the rig, nacelle, center pylon, and inboard surface junction region. The flow separation was caused by an adverse pressure gradient coupled with the corner flow in the region. The NATR center engine model was modified by reducing the length of the inboard surface upstream of the nozzle by 53% of the original chord length. The RANS simulation of the modified NATR center engine model showed that the region of separated flow was significantly reduced in size. Furthermore, the peak magnitude of turbulent kinetic energy produced by the flow separation was reduced by about 60%.

The RANS simulations were used to estimate the aerodynamic forces on the surfaces of the NATR models to help with the structural design of the models. The simulations showed that the forces were unsteady but seemed to fluctuate about a center value. The average aerodynamic forces were computed and found to be relatively small – significantly smaller than the expected forces experienced by the models due to their own weight.

The RANS simulations of the LM1044-3 aircraft were also used to assess the performance of the axisymmetric inlet. The simulations showed very good agreement with the total pressure recovery of 98.9% predicted previously in Reference 3. The simulations showed that the inlet has very low circumferential and radial distortion at take-off conditions. Furthermore, this study showed that as the angle of attack increased, neither inlet total pressure recovery or inlet distortion increase substantially.

Finally, the simulations did highlight the weakness of not refining the grid within the jet plume region. In this case, an unstructured grid was generated without placing grid in the nozzle jet plume. This oversight did not significantly affect the forces on the aircraft body. However, as the flow exited the nozzle, the jet quickly and unphysically ended. Since there was little grid to resolve the flow, there was no significant mixing or increase in turbulent kinetic energy in the shear layer as the jet mixed out. Resolving the jet plume region is paramount for simulations of jet-surface interactions and screening simulations of jet flows. But, the principle of smartly applied grid to sufficiently resolve regions of flow with significant gradients can be applied to a number of other flow features, including shockwaves and reacting flows.

VII. Appendix

Several years prior to the work discussed in this paper, Reynold-Averaged Navier-Stokes (RANS) simulations were conducted of a three-stream, inverted velocity profile (IVP) nozzle, similar to the nozzle discussed in Section III-B and used in the jet-surface interaction study. This three-stream IVP nozzle was designed to help reduce jet noise from a supersonic commercial transport aircraft on an airport community. The three-stream IVP nozzle was tested experimentally on the NASA Glenn Research Center Nozzle Acoustic Test Rig. Two sets of simulations were performed: pre-test screening simulations were performed prior to the isolated nozzle acoustics experiment; post-test simulations were performed using the actual nozzle and freestream conditions used in the acoustics experiment. The purpose of the pre-test RANS screening simulations was to verify that the nozzle flows were free of any potential sources of rig noise, such as flow separation or other forms of unsteady flow. The purpose of the post-test RANS simulations was to provide flow solutions for use as input into an acoustic analogy-based jet noise prediction code. The post-test RANS simulations will be presented here.

A. Nozzle Geometry

The three-stream IVP nozzle consisted of an inner stream, a primary stream, and a buffer stream. The primary stream – the largest stream – was composed of the mixed flows from the engine core stream and the secondary fan stream. A tertiary fan stream is split evenly to supply the inner stream and buffer stream. The inner stream and primary stream span the entire circumference of the nozzle; the buffer stream spans only the ground-side half of the circumference of the nozzle. The internal geometry of the IVP nozzles was proprietary, therefore the internal flowpaths will be concealed in all figures. The three stream nozzle had a geometry that varied throughout the flight envelop. Figure 31a and Figure 31b shows the external geometry for two IVP nozzle configurations, 'Sideline' and 'Cutback.' The primary difference between the two configurations is the streamwise location of the plug and inner stream nozzle exit: relative to the primary stream exit and buffer stream, the plug and inner stream exit are located further aft for the Cutback configuration than the Sideline configuration. The IVP nozzle simulations were compared to a baseline round, single-stream convergent nozzle, denoted as the 'C4' nozzle and pictured in Figure 31c, which was run at equivalent flow conditions.

B. Flow Conditions

Simulations of the three-stream IVP nozzle were performed at two different flow conditions, 'Sideline' and 'Cutback.' These nozzle conditions represent two engine cycles for which noise certification measurements would be taken. The Sideline condition represented the engine cycle shortly after take-off in which noise measurements would be taken from an observation point to the side of the flight path. The Cutback condition represents a lower power engine cycle used for noise abatement. The IVP nozzle conditions are listed in Table 7. The equivalent mixed-flow conditions used for the C4 baseline nozzle are also listed in Table 7. The equivalent conditions give the C4 nozzle the same jet velocity and temperature as the fully mixed flow from the IVP at the corresponding conditions. For the acoustic tests and jet-noise prediction code, the noise results were scaled by the nozzles' thrust. The freestream conditions used to match test conditions for each nozzle configuration are listed in Table 8. The freestream flow was set to Mach 0.3 for all cases.

Table 7: Nozzle flow conditions for inverted velocity profile and baseline nozzle simulations.

Nozzle Condition	Inner Stream NPR	Inner Stream NTR	Primary Stream NPR	Primary Stream NTR	Buffer Stream NPR	Buffer Stream NTR
IVP Sideline	1.780	1.390	2.014	2.077	1.780	1.390
C4 Sideline	-	-	1.929	1.777	-	-
IVP Cutback	1.638	1.290	1.557	1.776	1.638	1.290
C4 Cutback	-	-	1.582	1.582	-	-

Table 8: Freestream conditions for inverted velocity profile and baseline nozzle simulations.

Nozzle Simulation	p_∞ [psi]	T_∞ [°R]	M_∞
IVP Sideline	14.19	480.0	0.30
C4 Sideline	14.30	498.2	0.30
IVP Cutback	14.03	500.0	0.30
C4 Cutback	14.27	505.1	0.30

C. Flow Solver

All the simulations of the three-stream IVP nozzles were performed using Wind-US v3[14,15]. Wind-US is a general-purpose, RANS solver that can provide flow solutions for both structured and unstructured grids. The code is developed and managed by the NPARC Alliance, a partnership between NASA Glenn Research Center, USAF Arnold Engineering Development Complex, and The Boeing Company. Wind-US offers a variety of numerical schemes, as well as several zero-, one-, and two-equation turbulence models. These simulations used a second-order Roe numerical scheme and the Menter Shear Stress Transport (SST) turbulence model[5].

D. Structured Grids

Two three-dimensional structured grids were generated for the three-stream IVP nozzles, one each for the Sideline and Cutback configurations. The grids were generated with Pointwise[8]. The grids took advantage of each nozzle's symmetry and only modeled half of the nozzle flow. Viscous wall spacing was set to 0.0001 inches, to ensure a nominal y^+ value of 1.0 along the viscous surfaces. The grids extended 40 primary nozzle diameters (D_{pr}) in the radial direction and $50 \times D_{pr}$ downstream of the nozzle exit. A single two-dimensional axisymmetric grid was generated for the C4 baseline nozzle. It used similar grid spacing and grid dimensions as the IVP nozzle grids. The grids are pictured in Figure 32. The grid for the Sideline configuration was composed of 46.6 million cells; the grid for the Cutback configuration was composed of 47.4 million cells. The C4 nozzle grid consisted of 155,200 cells.

E. Results

The convergence of the solutions was determined by monitoring nozzle massflow and thrust and by monitoring flow quantities in the plume, such as streamwise velocity and turbulent kinetic energy. Typically, fluctuations in the nozzle massflow and thrust settled out more quickly than fluctuations in the jet plume.

1. Sideline

Contours of streamwise velocity and turbulent kinetic energy along the symmetry plane of the IVP Sideline case are plotted in Figure 33. The velocity and turbulent kinetic energy are both non-dimensionalized by the ideally expanded jet velocity of the primary nozzle, U_{jet}=1473 ft/s. For comparison, contours of velocity and turbulent kinetic energy of the C4 baseline nozzle using the equivalent Sideline condition are presented in Figure 34. Even though the actual ideally expanded jet velocity of the C4 Sideline conditions is U_{jet}=1349 ft/s, the velocity and turbulent kinetic energy are non-dimensionalized using U_{jet}=1473 ft/s from the IVP Sideline nozzle so the two cases can be compared. Comparing the streamwise velocity of the IVP Sideline and C4 Sideline nozzle simulations in Figure 33a and Figure34a, respectively, the IVP nozzle produces a shorter jet potential core than the C4 nozzle – approximately $5.6 \times D_{pr}$ when comparing the contours for $0.90 \times U_{jet}$. The buffer stream on the lower side of the IVP Sideline nozzle appears to reduce the velocity gradient acting upon the primary nozzle stream, allowing the core of the primary nozzle stream to extend further downstream on the lower side of the nozzle than it does on the upper side of the nozzle, about $1.6 \times D_{pr}$ when comparing the contours for $0.90 \times U_{jet}$. The reduced velocity gradient on the lower side, in turn, reduces the intensity of the turbulent kinetic energy on the lower side of the IVP nozzle in Figure 33b. The peak turbulent kinetic energy on the lower side of the IVP nozzle simulation is nearly the same as that of the C4 nozzle simulation (see Figure 34b) – $0.015 \times (U_{jet})^2$ – however the region of peak turbulent kinetic energy of the IVP nozzle plume is significantly shorter than that of the C4 nozzle. Whereas jet noise is directly proportional to turbulent kinetic energy, the IVP Sideline nozzle shows

potential to reduce jet noise from the lower side of the nozzle. However, Figure 33b also reveals a small, but intense, region of turbulent kinetic energy in the inner stream-primary stream shear layer, just downstream of the inner nozzle exit. A closer inspection of the velocity near the nozzle reveals that the primary stream flow separates from the nozzle splitter surface, likely due to an adverse pressure gradient as the splitter curves towards the nozzle centerline.

2. Cutback

Contours of the streamwise velocity and turbulent kinetic energy for the three-stream IVP nozzle and the C4 baseline nozzle using their respective Cutback flow conditions are shown in Figure 35 and Figure 36, respectively. The contours of streamwise velocity and turbulent kinetic energy are non-dimensionalized by U_{jet}=1126 ft/s for the C4 nozzle simulations. (The actual ideally-expanded jet velocity of the C4 nozzle using Cutback conditions is U_{jet}=1086 ft/s.) As with the Sideline simulations, the lower side of IVP nozzle jet core is about $4.2 \times D_{pr}$ shorter than the C4 nozzle jet core when comparing the contours for $0.90 \times U_{jet}$. Unlike the IVP nozzle Sideline simulation, as observed in Figure 35a, the top side of the primary stream potential core extends about $0.4 \times D_{pr}$ further downstream than the lower side of the potential core. The plot of turbulent kinetic energy in Figure 35b, shows that the buffer stream of the IVP nozzle does have a significant effect, delaying the onset of magnitude of peak turbulent kinetic energy on the lower side of the jet. As with the Sideline simulations, the lower side of jet plumes for the IVP nozzle and the C4 nozzle at cutback conditions have peak turbulent kinetic energies that are similar in magnitude – about $0.014 \times (U_{jet})^2$ – but the region of peak turbulent kinetic energy is much smaller for the IVP nozzle than the C4 nozzle. At the Cutback conditions, there is no apparent flow separation from the inner stream nozzle splitter.

F. Summary

Reynolds-Averaged Navier-Stokes (RANS) simulations were completed for two configurations of a three-stream inverted velocity profile (IVP) nozzle and a baseline single-stream round nozzle (mixed-flow equivalent conditions). For the Sideline and Cutback flow conditions, while the IVP nozzles did not reduce the peak turbulent kinetic energy on the lower side of the jet plume, the IVP nozzles did significantly reduce the size of the region of peak turbulent kinetic energy when compared to the jet plume of the baseline nozzle cases. The IVP nozzle at Sideline conditions did suffer a region of separated flow from the inner stream nozzle splitter that did produce an intense, but small, region of turbulent kinetic energy in the vicinity of the nozzle exit. When viewed with the understanding that jet noise is directly related to turbulent kinetic energy, these IVP nozzle simulations show the potential to reduce noise to observers located below the nozzle. However, these RANS simulations also show that some modifications may be needed to prevent the small region of separated flow-induced turbulent kinetic energy from the inner stream nozzle splitter at Sideline conditions.

VIII. Acknowledgements

IX. References

[1] NASA Aeronautics Strategic Implementation Plan [webpage],
URL: http://www.aeronautics.nasa.gov/strategic-plan.htm, [cited 18 October 2016].

[2] Bridges, J., Podboy, G. G., and Brown, C. A., "Testing Installed Propulsion for Shielded Exhaust Configurations," AIAA Paper 2016-3042, May 2016.

[3] Morgenstern, J., et al, "Advanced Concept Studies for Supersonic Commercial Transports Entering Service in the 2018-2020 Period, Phase 2," NASA/CR—2015-218719, July 2015.

[4] Biedron, R. T., et al, "FUN3D Manual: 12.7," NASA/TM—2015-218761, May 2015.

[5] Menter, F. R., "Two-Equation Eddy Viscosity Turbulence Models for Engineering Applications," *AIAA Journal*, Vol. 32, No. 8 (1994), pp. 1598-1605. doi: 10.2514/3.12149.

[6] Roe, P. L., "Approximate Riemann Solvers, Parameter Vectors, and Difference Schemes," Journal of Computational Physics, Vol. 43, 1981, pp. 357-372.

[7] Van Leer, B., "Flux-Vector Splitting for the Euler Equations," ICASE Report 82-30, 1982.

[8] Pointwise® [software package], Ver. 17.1 Release 4, Pointwise, Inc., Fort Worth, TX, 2013.

[9] "AFLR3, Version 15.5.5," CAVS SimCenter, Mississippi State University, Starkville, MS, 2015.

[10] Marcum, D. L. and Weatherill, N. P., "Unstructured Grid Generation Using Iterative Point Insertion and Local Reconnection," AIAA Journal, Vol. 33, No.9, pp. 1619-1625, September 1995.

[11] Marcum, D. L., "Unstructured Grid Generation Using Automatic Point Insertion and Local Reconnection," The Handbook of Grid Generation, edited by J. F. Thompson, B. Soni, and N. P. Weatherill, CRC Press, pp. 18-1 thru 18-31, 1998.

[12] NASA High-End Computing Capability [webpage], URL: http://www.nas.nasa.gov/hecc/, [cited 18 October 2016].

[13] Moore, M. T., "Distortion Data Analysis," AFAPL-TR-72-111, February 1973.

[14] Yoder, D. A., "Wind-US User's Guide Version 3.0," NASA/TM—2016-219078, March 2016.

[15] Georgiadis, N. J., Yoder, D. A., Towne, C. S., Engblom, W. A., Bhagwandin, V. A., Power, G. D., Lankford, D. W., and Nelson, C. C., "Wind-US Code Physical Modeling Improvements to Complement Hypersonic Testing and Evaluation," AIAA Paper 2009-193, Jan. 2009.

X. Figures

Figure 1: LM1044-3 commercial supersonic transport aircraft concept by Lockheed Martin[3].
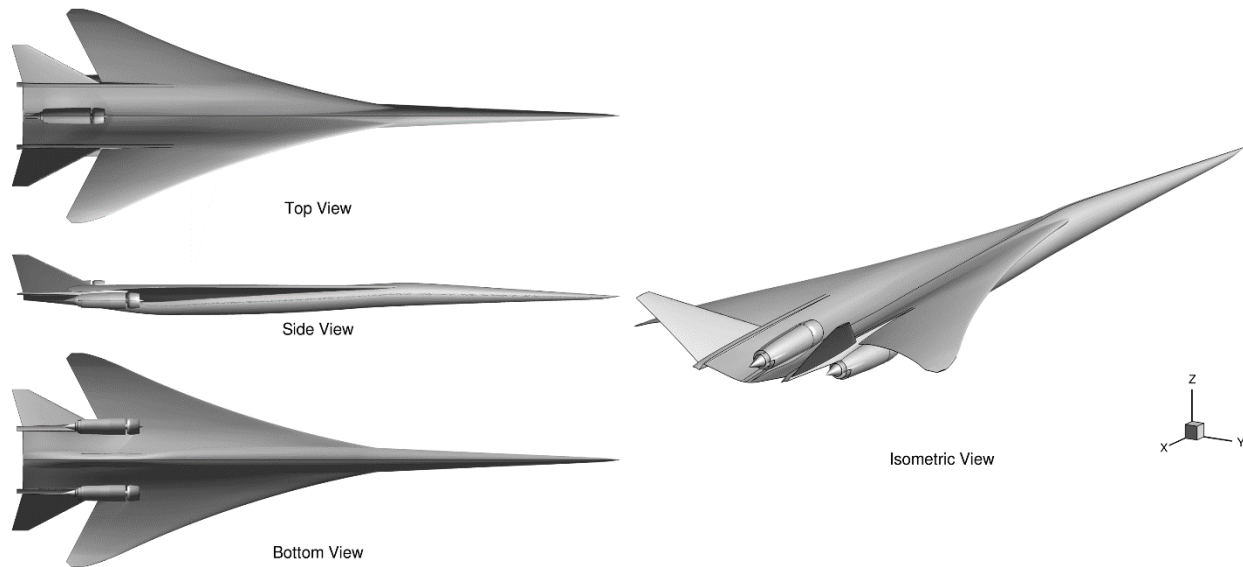
Figure 2. LM1044-3 geometry.
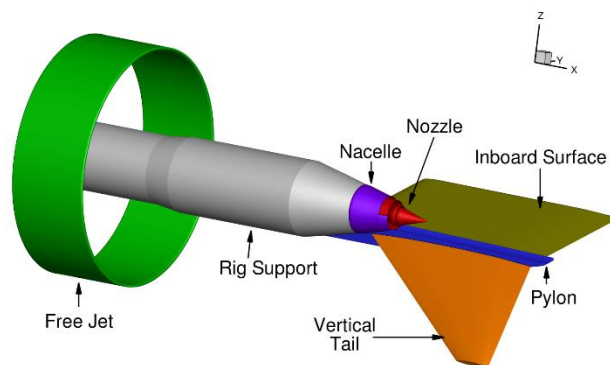
Figure 3. NATR outboard engine configuration geometry and nomenclature.

a) Original configuration.

b) Modified configuration.
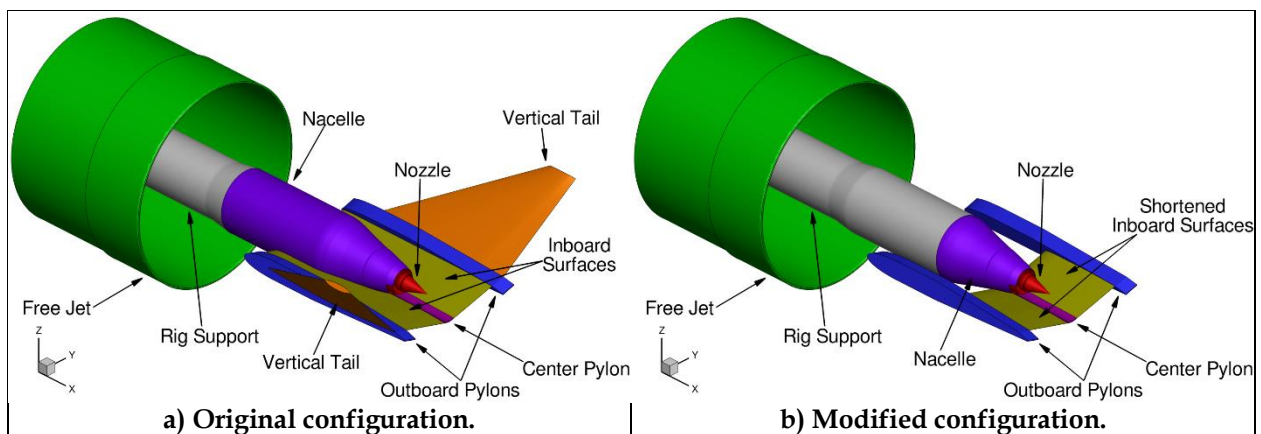
Figure 4. NATR center engine configuration geometry and nomenclature.

a) Full aircraft.
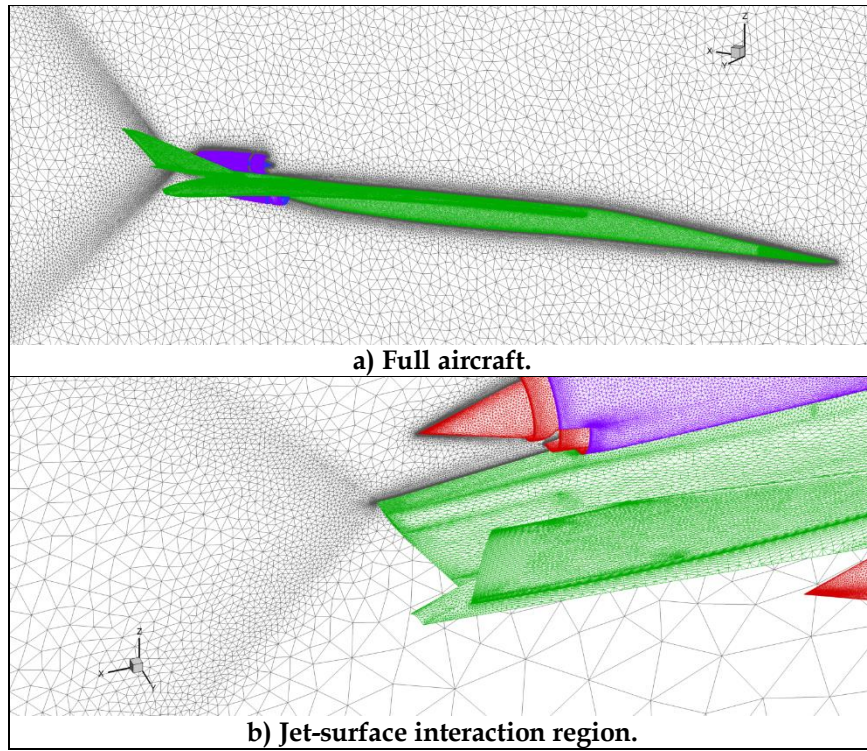
b) Jet-surface interaction region.
Figure 5: Grid for LM1044-3 aircraft.

a) Full aircraft.
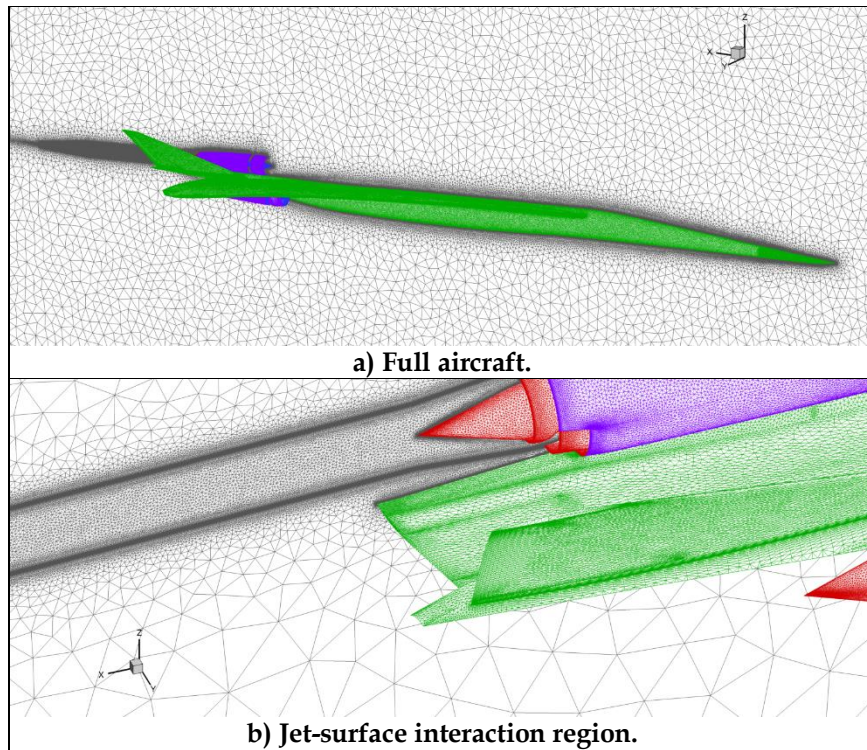
b) Jet-surface interaction region.
Figure 6: Grid for LM1044-3 aircraft with refined jet plumes.

| a) Full experimental model. | b) Jet-surface interaction region. |
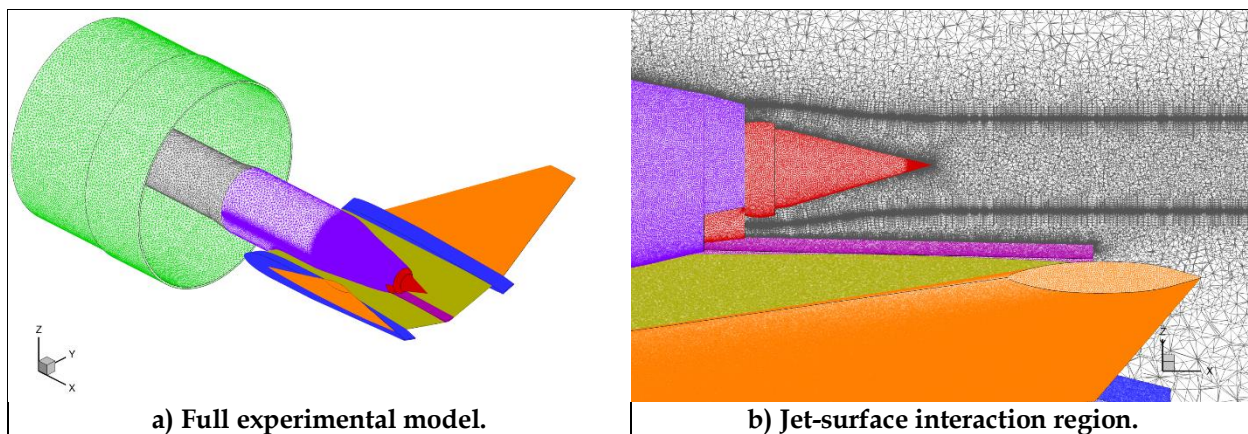
Figure 7: Grid for NATR center engine configuration.

| a) Full experimental model. | b) Jet-surface interaction region. |
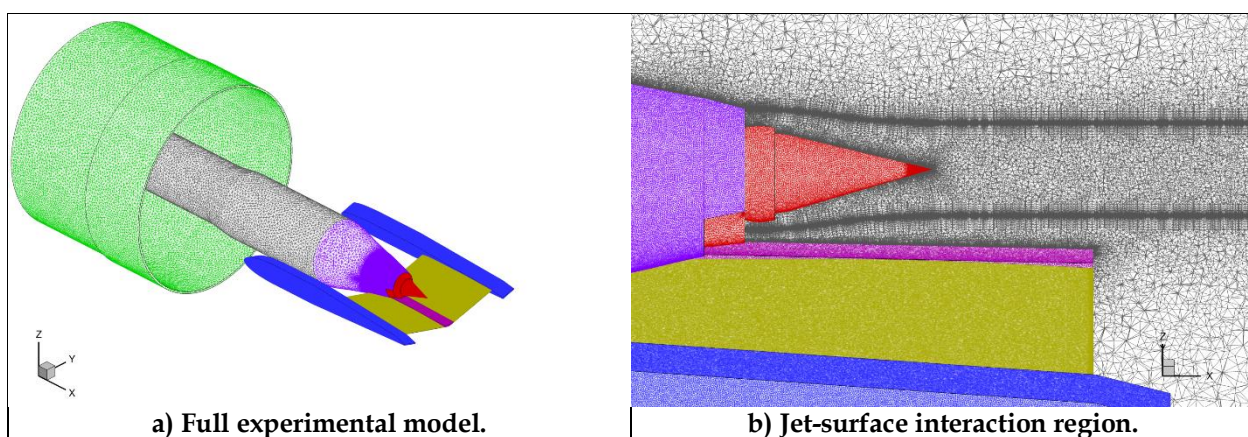
Figure 8: Grid for modified NATR center engine configuration.

| a) Full experimental model. | b) Jet-surface interaction region. |
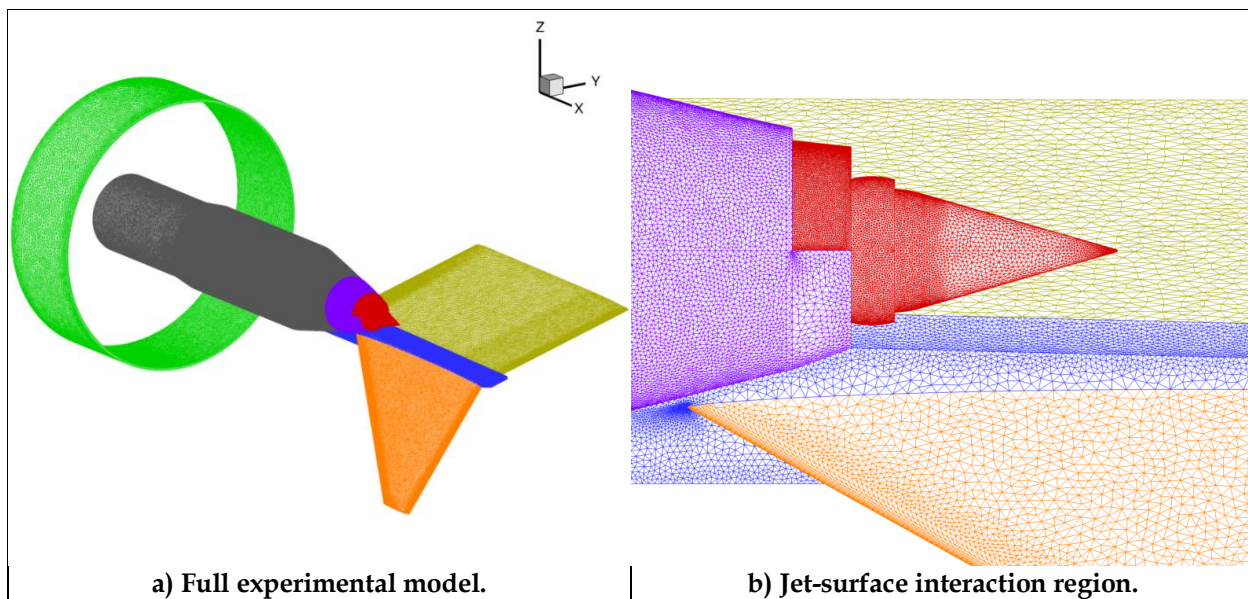
Figure 9: Grid for NATR outboard engine configuration.

American Institute of Aeronautics and Astronautics
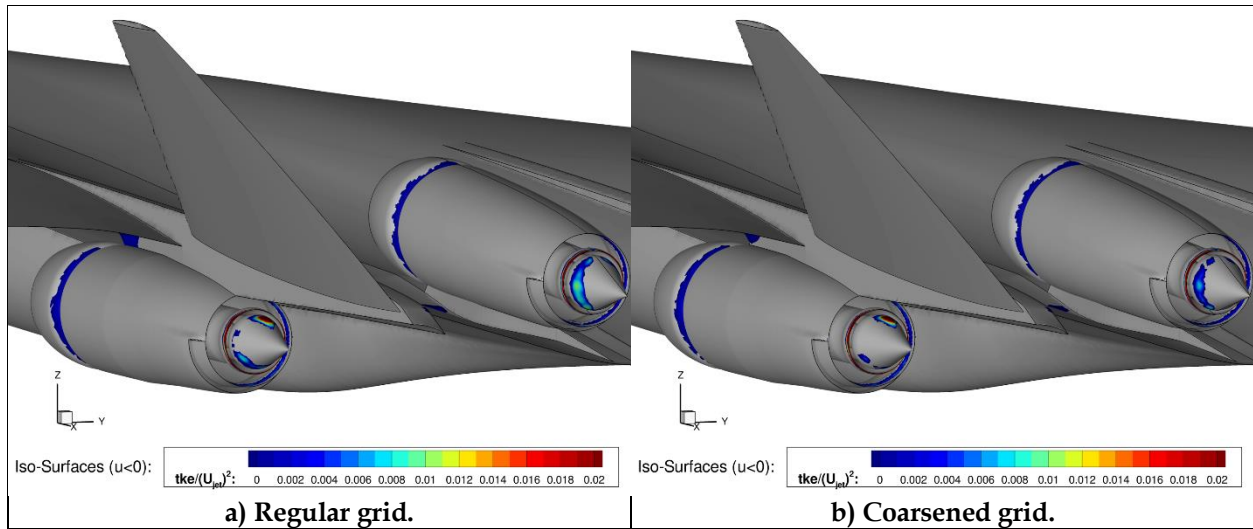
Figure 10: Comparison of flow separation near aft portion of LM1044-3 aircraft for regular and coarsened grids. U_{jet}=1469 ft/s.
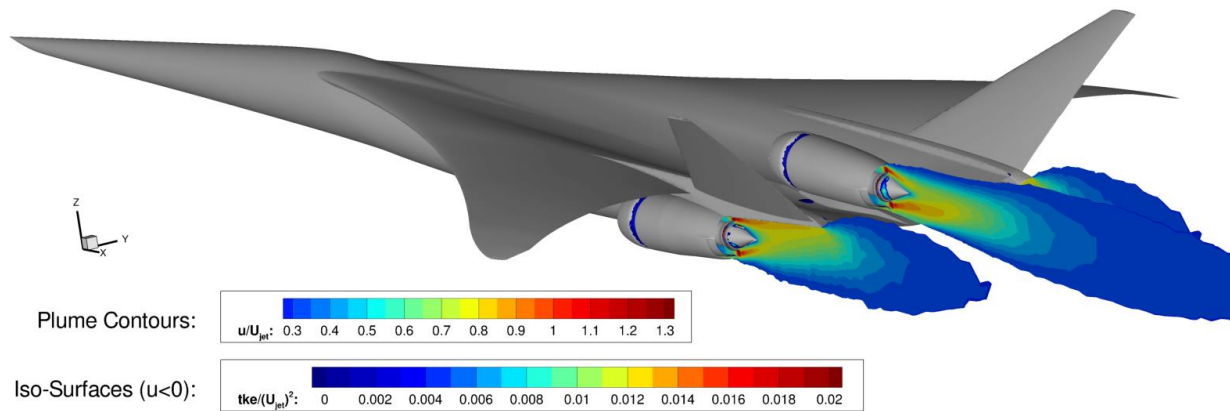
Figure 11: Contours of streamwise velocity through center plane of each engine of LM1044-3 aircraft. Iso-surfaces indicate separated flow and are colored by turbulent kinetic energy contours. U_{jet}=1469 ft/s.
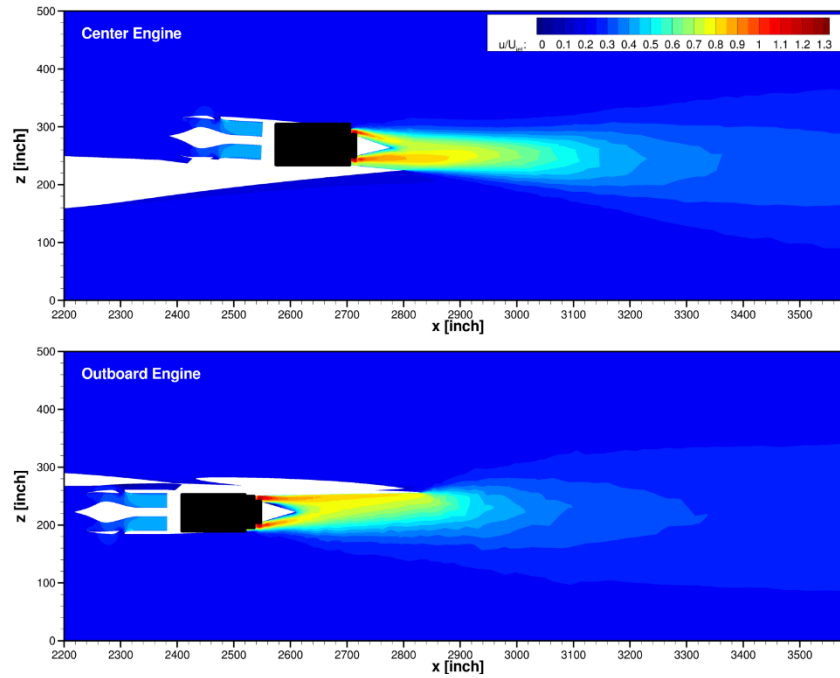
Figure 12: Contours of streamwise velocity through centerplane of each engine of LM1044-3 aircraft. U_{jet}**=1469 ft/s.**
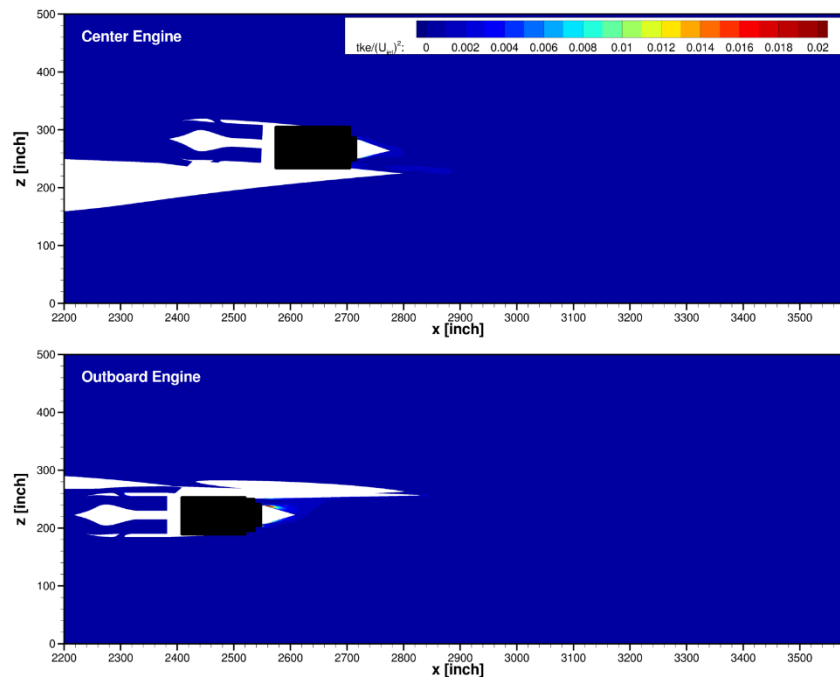
Figure 13: Contours of turbulent kinetic energy through centerplane of each engine of LM1044-3 aircraft. U_{jet}**=1469 ft/s.**
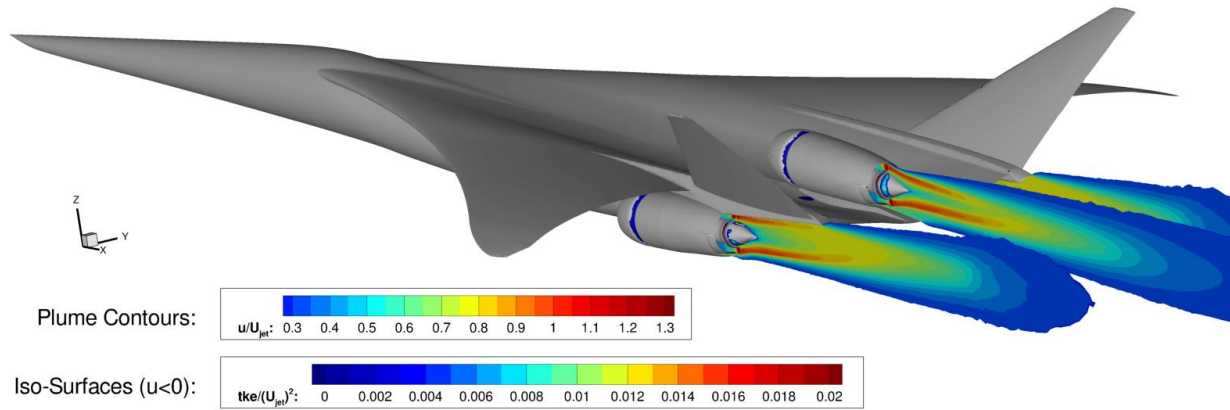
Figure 14: Contours of streamwise velocity through center plane of each engine of LM1044-3 aircraft with refined plume grid. Iso-surfaces indicate separated flow and are colored by turbulent kinetic energy contours. U_{jet}=1469 ft/s.
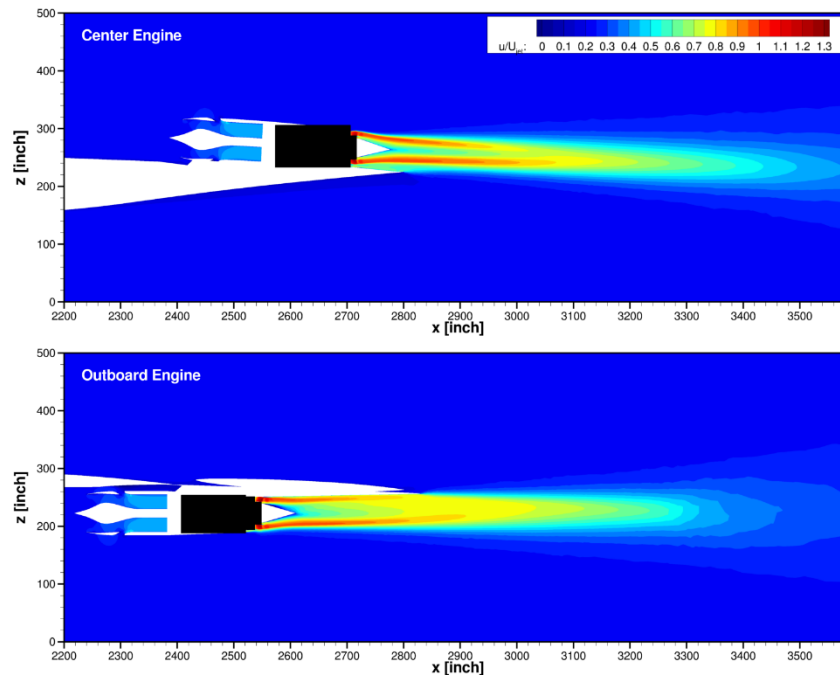
Figure 15: Contours of streamwise velocity through centerplane of each engine of LM1044-3 aircraft with refined plume grid. U_{jet}=1469 ft/s.

American Institute of Aeronautics and Astronautics
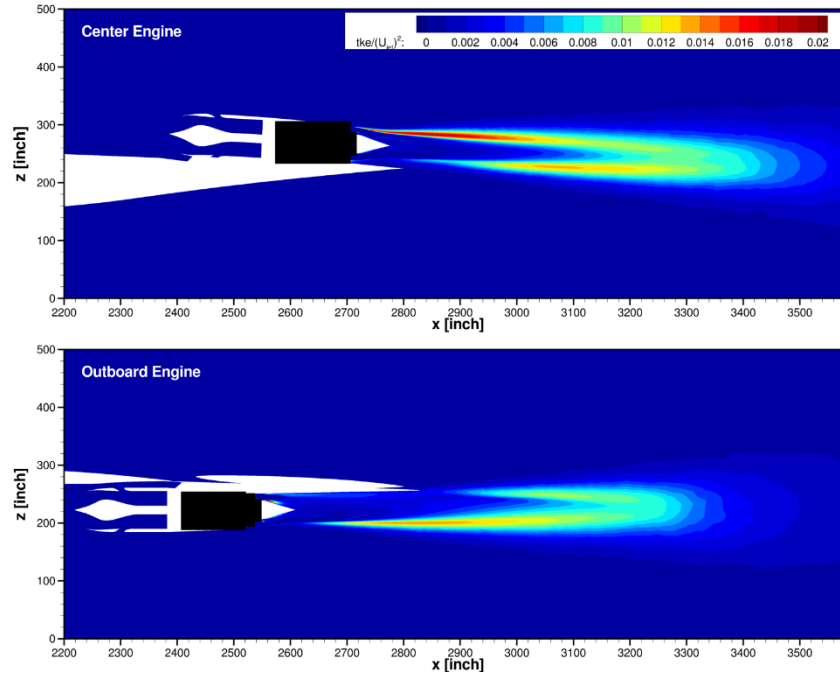
Figure 16: Contours of turbulent kinetic energy through centerplane of each engine of LM1044-3 aircraft with refined plume grid. U_{jet}=1469 ft/s.
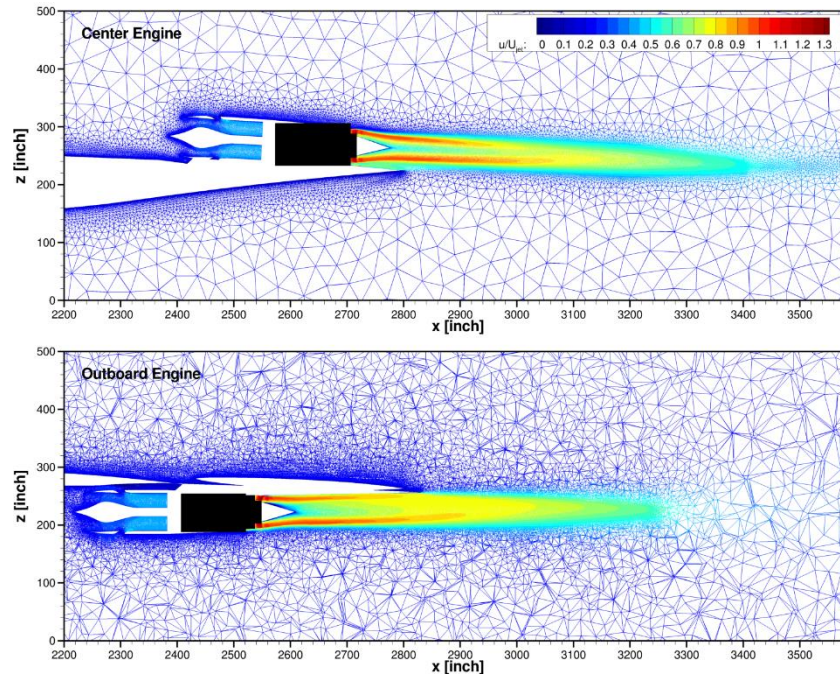
Figure 17: Grid of LM1044-3 aircraft with refined plume, colored by contours of streamwise velocity through centerplane of each engine. U_{jet}=1469 ft/s.

American Institute of Aeronautics and Astronautics
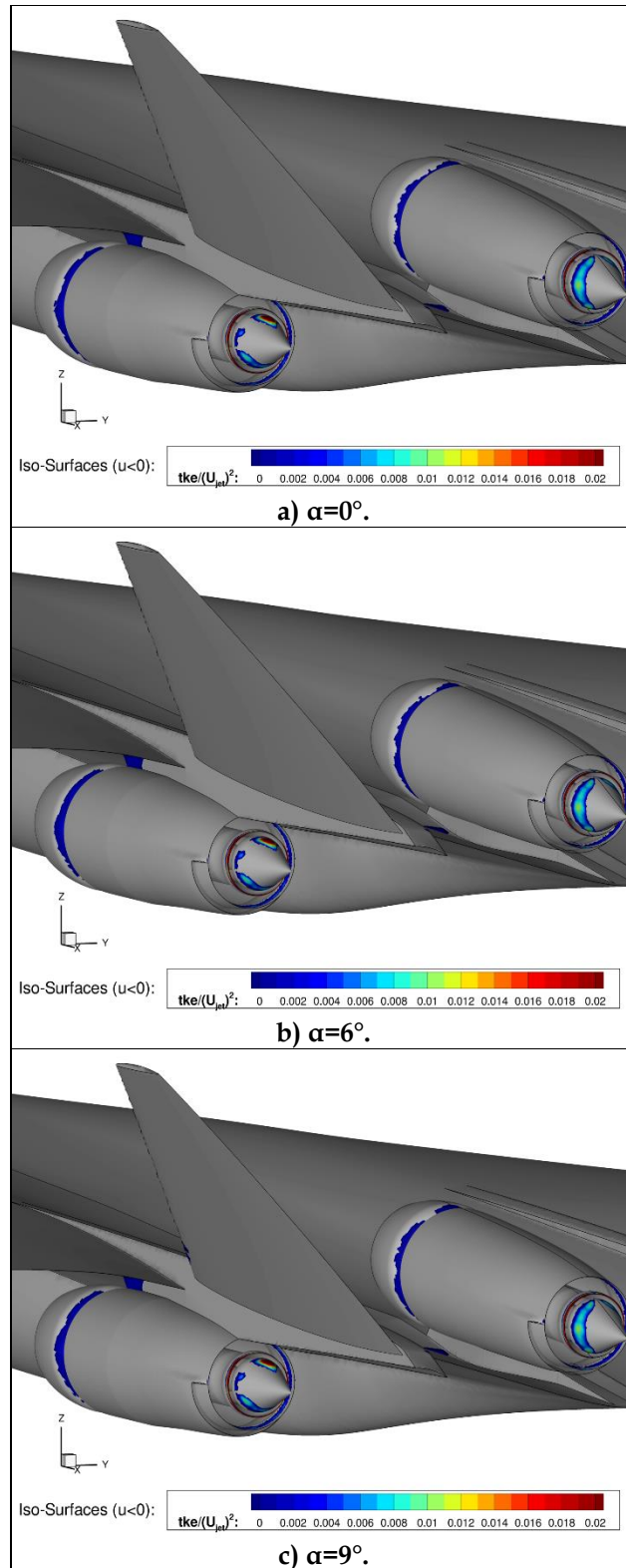
Figure 18: Comparison of flow separation near aft portion of LM1044-3 aircraft as angle of attack is increased. U_{jet}=1469 ft/s.

a) α=0°.

b) α=6°.

c) α=9°.
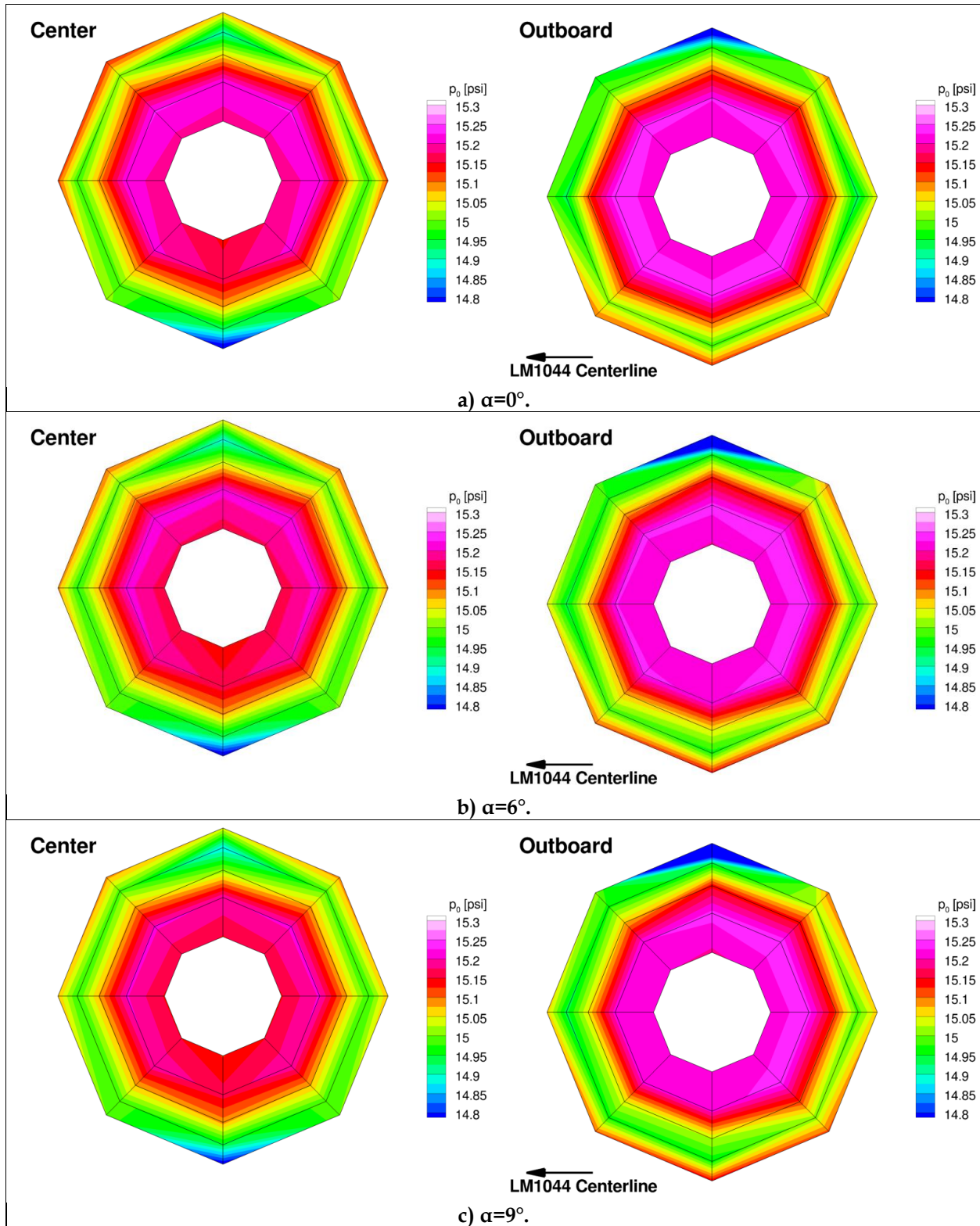
Figure 19: Total pressure at aerodynamic interface planes of center and outboard inlets as angle of attack is increased.

American Institute of Aeronautics and Astronautics

a) Steady-state (local time step) simulation. | **b) Time accurate (global time step) simulation.**
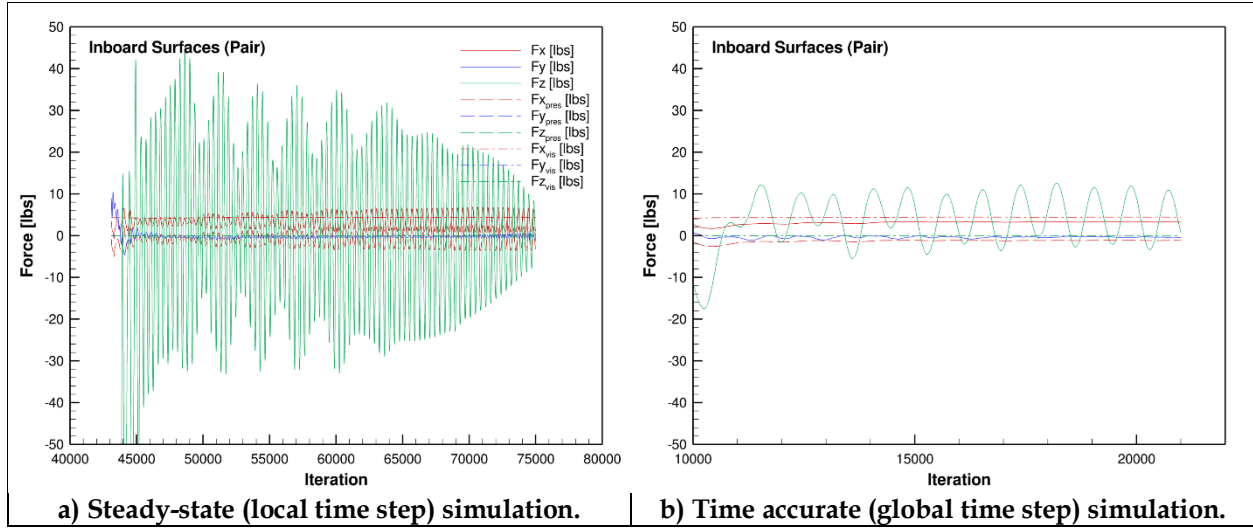
Figure 20: Convergence of aerodynamic loads on the NATR center engine configuration inboard surfaces.
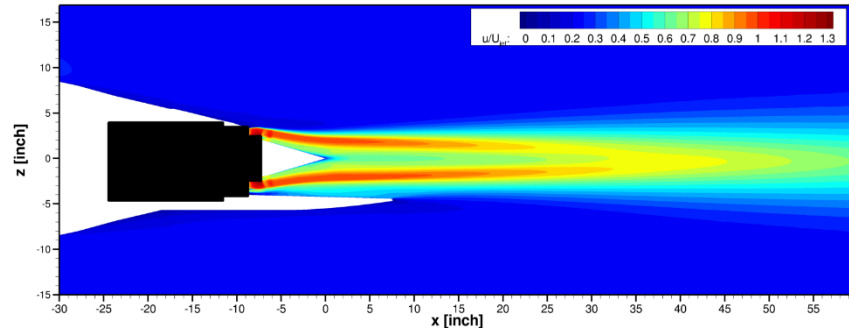
Figure 21: Contours of streamwise velocity along the center plane of the NATR center engine configuration. U_{jet}=1469 ft/s.
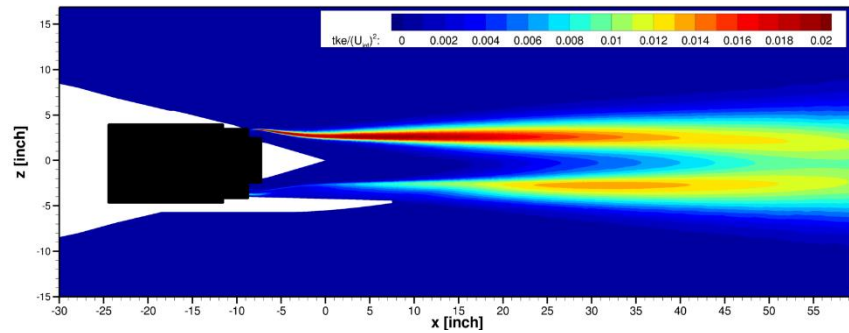
Figure 22: Contours of turbulent kinetic energy along the center plane of the NATR center engine configuration. U_{jet}=1469 ft/s.
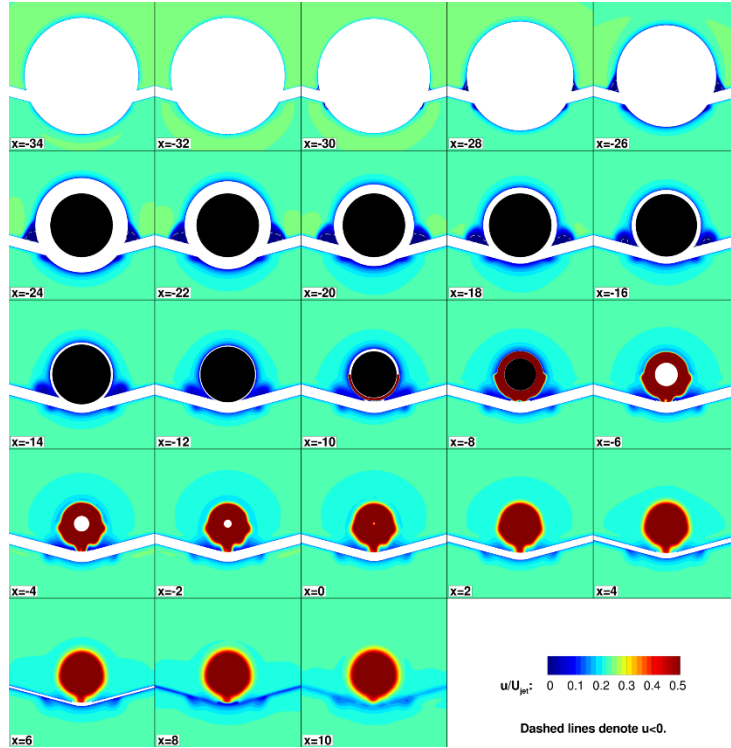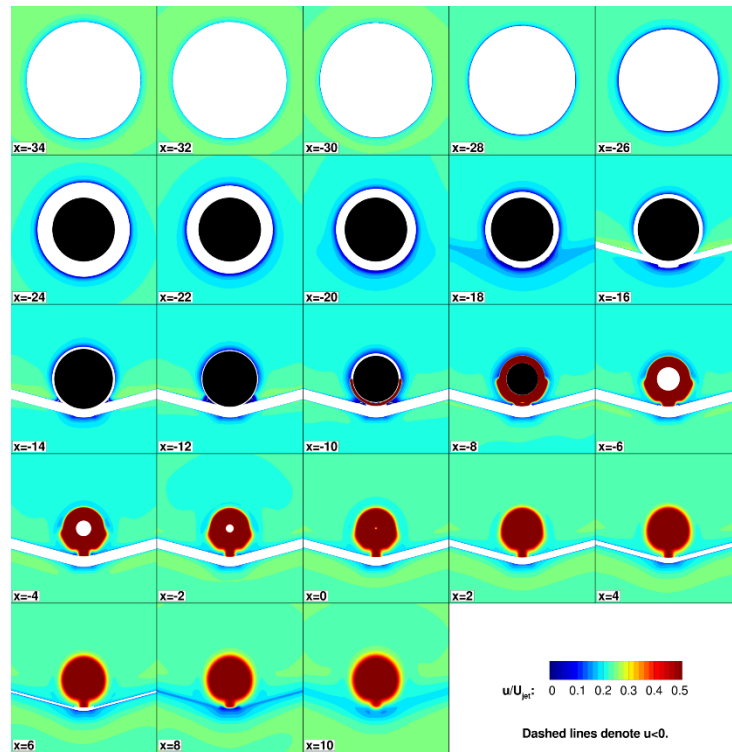
Figure 23: Contours of streamwise velocity at cross-planes of the NATR center engine configuration.
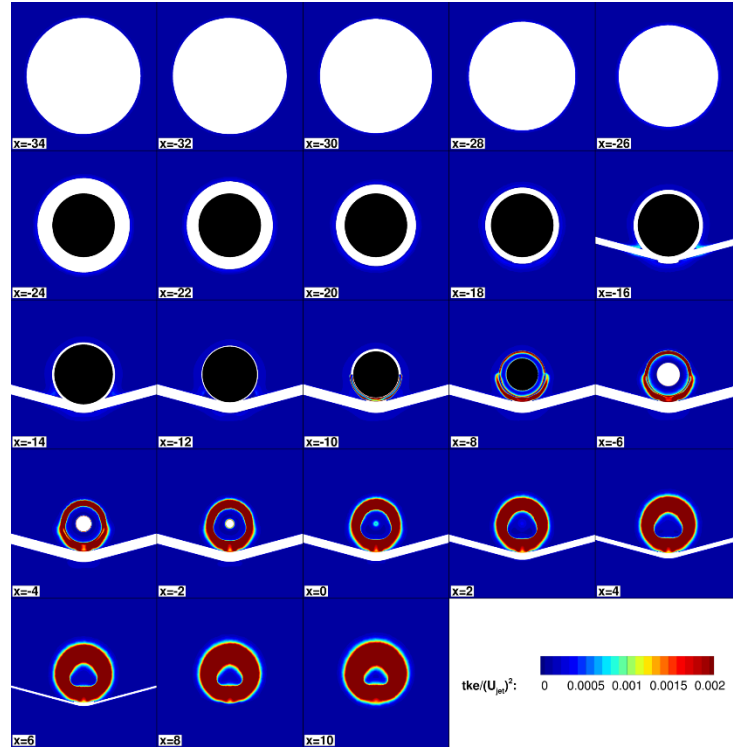U_{jet}=1469 ft/s. Cross-plane locations are given in inches.
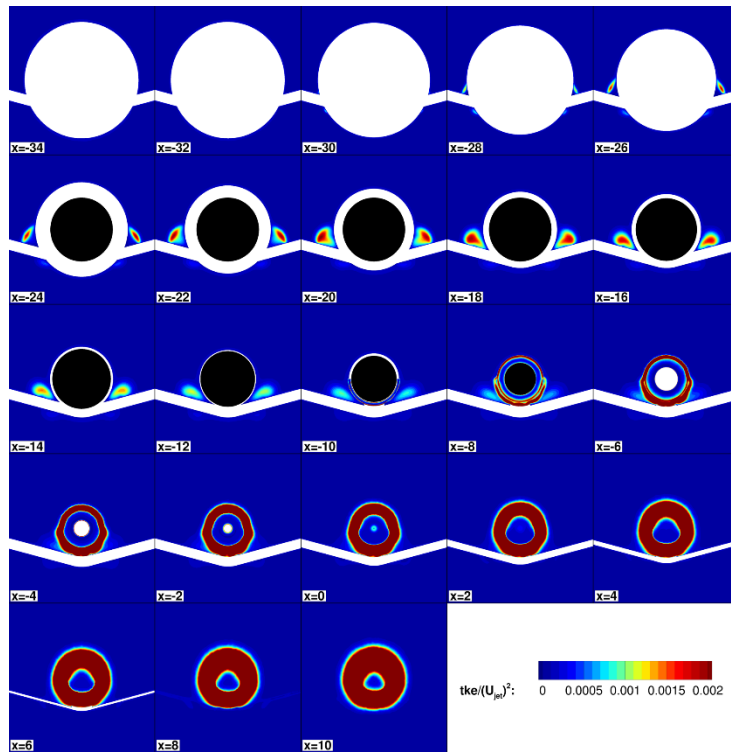
Figure 24: Contours of turbulent kinetic energy at cross-planes of the NATR center engine configuration. U_{jet}=1469 ft/s. Cross-plane locations are given in inches.
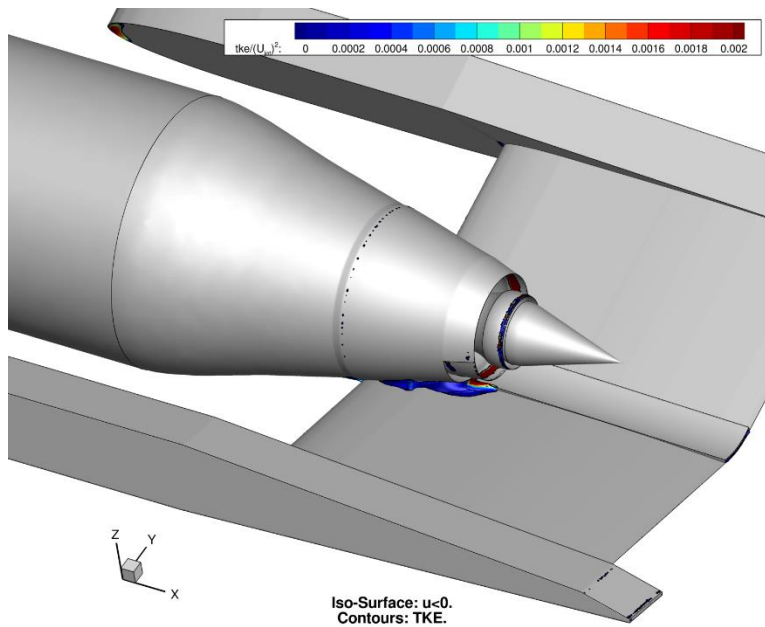
American Institute of Aeronautics and Astronautics
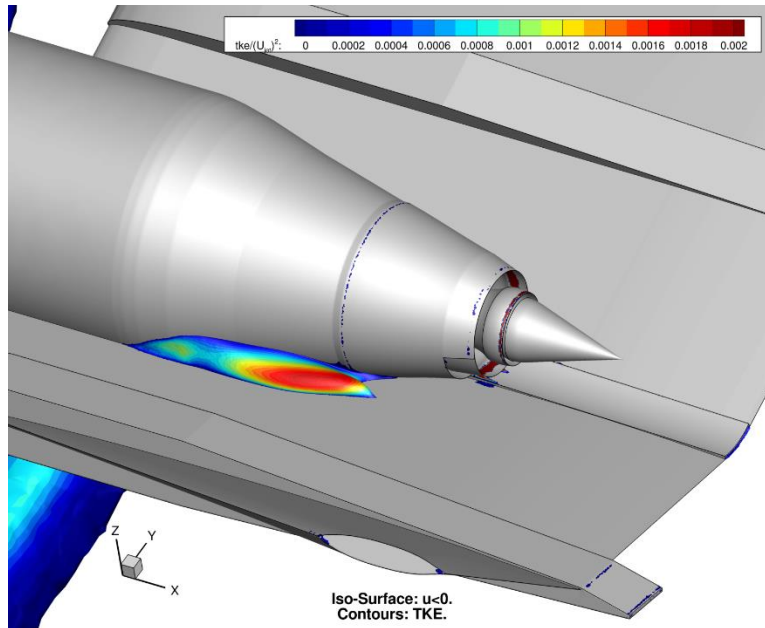
Figure 25: Iso-surface depicting separated flow along the NATR center engine configuration. Iso-surfaces are colored by turbulent kinetic energy contour levels. U_{jet}=1469 ft/s.

Figure 26: Contours of streamwise velocity at cross-planes of the modified NATR center engine configuration. U_{jet}=1469 ft/s. Cross-plane locations are given in inches.

Figure 27: Contours of turbulent kinetic energy at cross-planes of the modified NATR center engine configuration. U_{jet}=1469 ft/s. Cross-plane locations are given in inches.

Figure 28: Iso-surface depicting separated flow along the modified NATR center engine configuration. Iso-surfaces are colored by turbulent kinetic energy contour levels. U_{jet}=1469 ft/s.
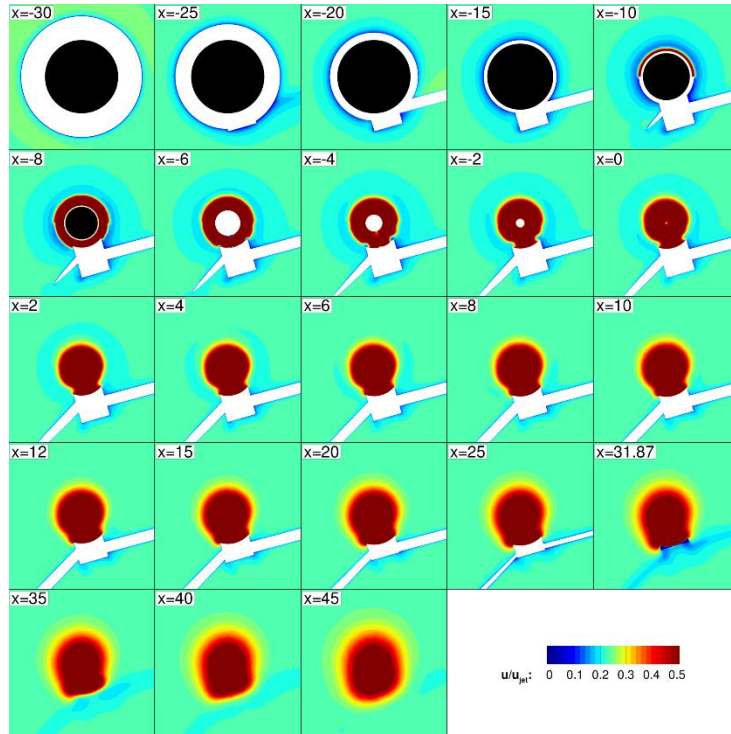
American Institute of Aeronautics and Astronautics

Figure 29: Streamwise velocity profiles for the NATR outboard engine configuration. U_{jet}=1469 ft/s. Cross-plane locations are given in inches.
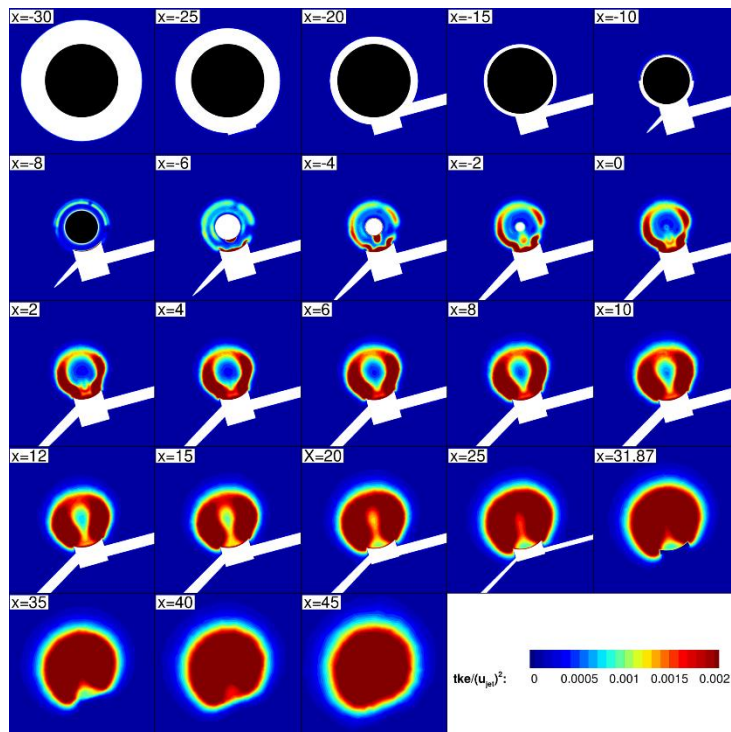

Figure 30: TKE profiles for the NATR outboard engine configuration. U_{jet}=1469 ft/s. Cross-plane locations are given in inches.
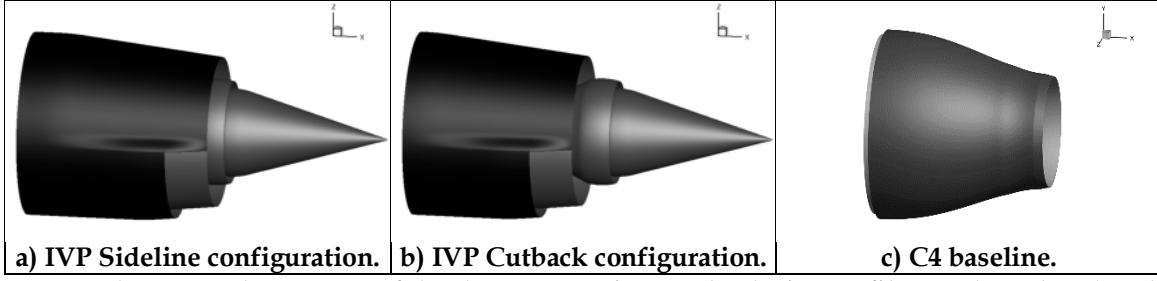
American Institute of Aeronautics and Astronautics

a) IVP Sideline configuration.   b) IVP Cutback configuration.   c) C4 baseline.

Figure 31: The external geometry of the three-stream inverted velocity profile nozzle and C4 baseline nozzle.

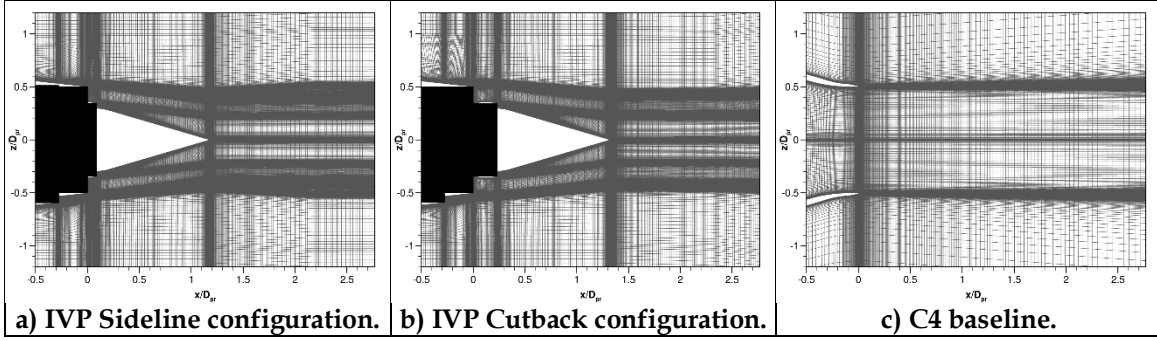a) IVP Sideline configuration.   b) IVP Cutback configuration.   c) C4 baseline.

Figure 32: Grids for the Sideline and Cutback configurations of the three-stream inverted velocity profile nozzle and C4 baseline nozzle.

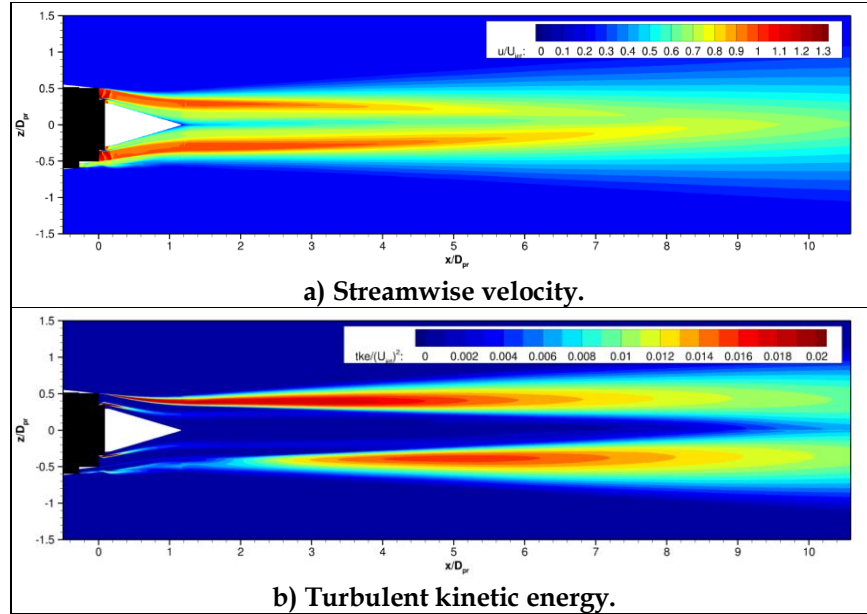a) Streamwise velocity.

b) Turbulent kinetic energy.

Figure 33: Contours of streamwise velocity and turbulent kinetic energy for the Sideline configuration of the three-stream inverted velocity profile nozzle. U_{jet}=1473 ft/s.

American Institute of Aeronautics and Astronautics

a) Streamwise velocity.
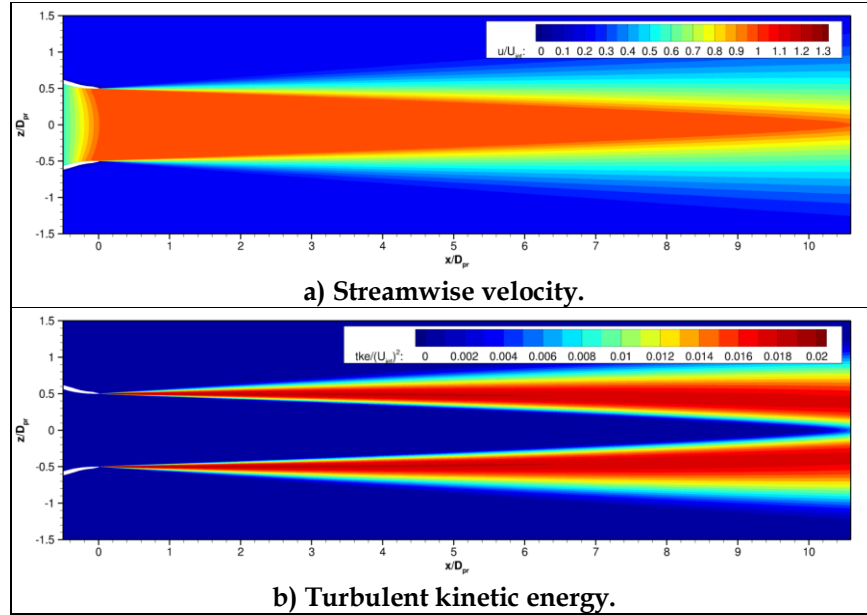

b) Turbulent kinetic energy.

Figure 34: Contours of streamwise velocity and turbulent kinetic energy for the C4 baseline nozzle at equivalent Sideline conditions. U_{jet}=1473 ft/s.

a) Streamwise velocity.

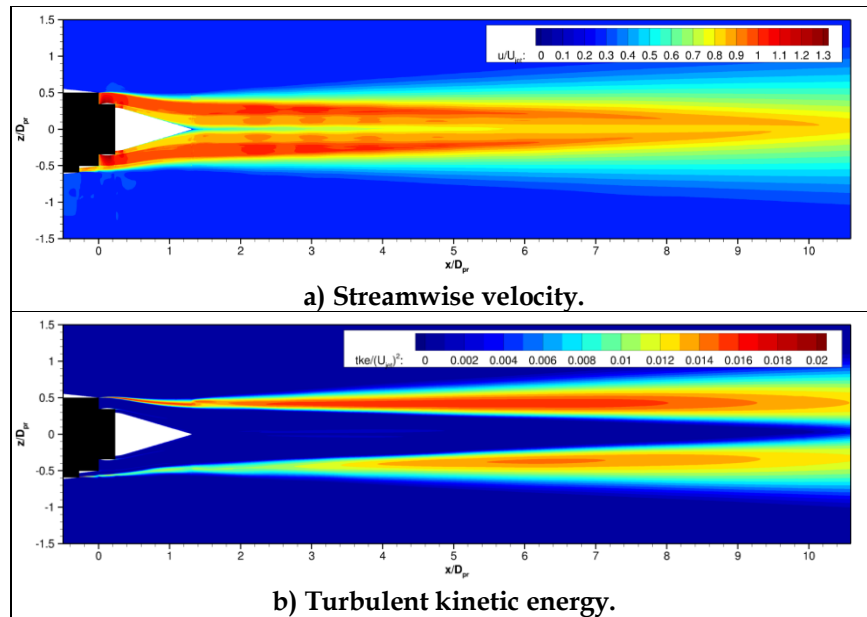**b) Turbulent kinetic energy.**

Figure 35: Contours of streamwise velocity and turbulent kinetic energy for the Cutback configuration of the three-stream inverted velocity profile nozzle. U_{jet}=1126 ft/s.

American Institute of Aeronautics and Astronautics

a) Streamwise velocity.

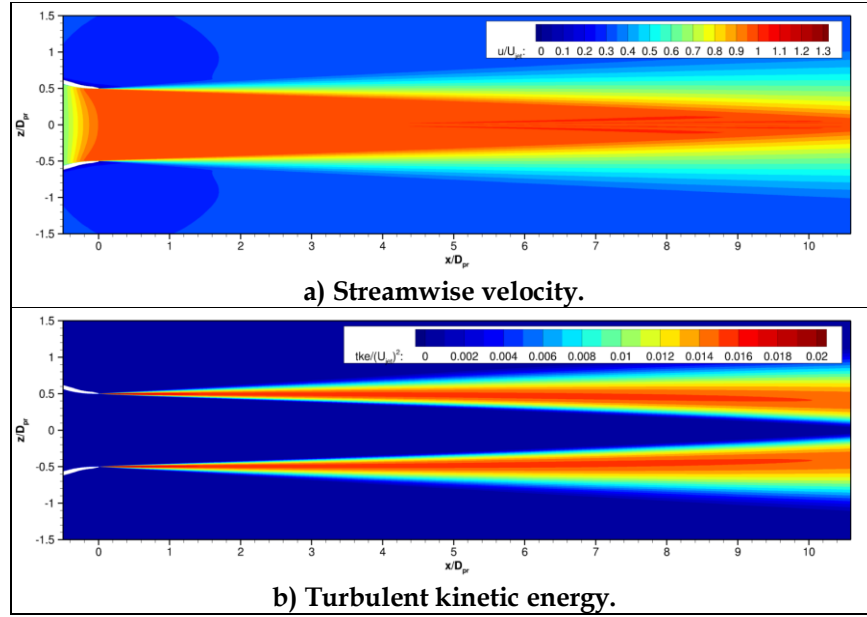**b) Turbulent kinetic energy.**

Figure 36: Contours of streamwise velocity and turbulent kinetic energy for the C4 baseline nozzle at equivalent Cutback conditions. U_{jet}=1126 ft/s.